Seismic signatures of fluctuating fragmentation in volcanic eruptions

Katherine R. Coppess[1], Fredric Y. K. Lam[2], Eric M. Dunham[2,3]

[1]Department of Physics, Stanford University, CA, USA
[2]Institute for Computational and Mathematical Engineering, Stanford University, Stanford, CA, USA
[3]Department of Geophysics, Stanford University, CA, USA

Key Points:

- Fluctuations in magma fragmentation during explosive volcanic eruptions change forces exerted on solid Earth and generate seismic waves
- We compute synthetic seismograms from unsteady conduit flow models of high viscosity magma parcels passing through fragmentation
- Stochastic fluctuations in fragmentation might explain eruption tremor that is ubiquitously observed during explosive volcanic eruptions

Corresponding author: Eric M. Dunham, edunham@stanford.edu

Abstract

Fragmentation plays a critical role in eruption explosivity by influencing the eruptive jet and plume dynamics that may initiate hazards such as pyroclastic flows. The mechanics and progression of fragmentation during an eruption are challenging to constrain observationally, limiting our understanding of this important process. In this work, we explore seismic radiation associated with unsteady fragmentation. Seismic force and moment tensor fluctuations from unsteady fragmentation arise from fluctuations in fragmentation depth and wall shear stress (e.g., from viscosity variations). We use unsteady conduit flow models to simulate perturbations to a steady-state eruption from injections of heterogeneous magma (specifically, variable magma viscosity due to crystal volume fraction variations). Changes in wall shear stress and pressure determine the seismic force and moment histories, which are used to calculate synthetic seismograms. We consider three heterogeneity profiles: Gaussian pulse, sinusoidal, and stochastic. Fragmentation of a high-crystallinity Gaussian pulse produces a distinct very-long-period (VLP) seismic signature and associated reduction in mass eruption rate, suggesting joint use of seismic, infrasound, and plume monitoring data to identify this process. Simulations of sinusoidal injections quantify the relation between the frequency or length scale of heterogeneities passing through fragmentation and spectral peaks in seismograms, with velocity seismogram amplitudes increasing with frequency. Stochastic composition variations produce stochastic seismic signals similar to observed eruption tremor, though computational limitations restrict our study to frequencies less than 0.25 Hz. We suggest that stochastic fragmentation fluctuations could be a plausible eruption tremor source.

Plain Language Summary

Explosive volcanic eruptions can be monitored and studied using seismic recordings of ground shaking produced by the eruption. This study explores the seismic expression of magma fragmentation. Fragmentation refers to magma breaking apart, a process that occurs in the upper part of volcanic conduits. Fragmentation reduces drag on the conduit walls and allows magma to erupt explosively. When fragmentation occurs in an unsteady manner, the forces exerted by the magma on the solid Earth change, producing seismic wave radiation. We use computer simulations of explosive eruptions and the accompanying seismic radiation to identify seismic signatures of fragmentation. Our results can help guide interpretation of seismic data from real eruptions, providing insight into controls on eruption explosivity.

1 Introduction

One of the primary controls on the explosivity of an eruption is fragmentation: the process by which magma breaks apart, leaving imbalanced forces that produce huge upward acceleration of the magma. However, there are still open questions about this process in regards to the mechanics and progression of fragmentation over the course of an explosive eruption. Unsteady fragmentation may lead to unsteady discharge, influencing eruption jet and plume dynamics which in turn affect aviation hazards from ash delivery to the atmosphere. In addition, it is possible that these variations could initiate column collapse and pyroclastic flows, posing significant hazards to surrounding communities.

Fragmentation marks the transition from a melt-continuous regime – with high drag along the conduit walls – to a gas-continuous regime – with drag becoming negligible. Seismology offers a potential way to provide quantitative constraints on this eruptive process, as the sudden changes in drag associated with fragmentation may excite seismic waves in the surrounding earth. As we will discuss in more detail later, it is arguable that unsteady fragmentation contributes to seismic radiation ranging from very long period (VLP, 0.01 to 0.5 Hz) frequencies to >1 Hz eruption tremor, depending on the timescales

of unsteadiness. Coherent VLP signals and stochastic tremor are universally observed during explosive eruptions but it is still not clear how to quantitatively interpret them. Eruption tremor in particular has been related empirically to plume height (McNutt, 1994; Prejean & Brodsky, 2011; Caplan-Auerbach et al., 2010) but the relation appears to be complex (Fee, Izbekov, et al., 2017). Numerical modeling provides a useful tool to explore these complex dynamics.

Evidence indicating that unsteady fragmentation could yield observable seismic signals is seen in Section 6 of Coppess et al. (2022). In that study, synthetic seismograms were calculated from unsteady conduit flow models. Simulations with insufficient spatial resolution in the finite difference discretization led to the halting descent of the fragmentation front (shown in their Figure 14). With insufficient resolution of the characteristic length scale of fragmentation, parcels of magma do not continuously fragment because conditions required for fragmentation have not yet been met. This means that drag between the parcel and the conduit walls remains high. As a result, the high drag reduces the flow speed and overpressure develops below the fragmentation front. Fragmentation then occurs at one grid point, releasing a high frequency seismic wave. The process repeats at subsequent grid points. While the source of the halting fragmentation front was numerical, the system responded in a realistic fluid dynamical way with high acceleration of melt due to the driving pressure gradient left behind when the restraining drag force was suddenly reduced. This response is captured in variations in shear stress on the conduit walls that lead to high frequency seismic wave radiation (see their Figure 15). In this current study, we revisit the problem of fluctuating fragmentation with well-resolved simulations and realistic causes of fluctuations.

One physically motivated source of unsteady fragmentation is heterogeneity in magma composition. Magma composition plays an important role in fluid dynamics through the magma viscosity, which determines how magma behaves in response to applied stresses. Magma viscosity depends on its bulk chemical composition, volatile content, and crystal content (e.g., Hess & Dingwell, 1996; Costa, 2005; Gonnermann, 2015). This enters our conduit flow modeling through the shear stress between the magma and the conduit walls, which increases with increasing magma viscosity for the same ascent rate. Therefore, variations in magma composition yield (potentially sudden) changes in wall shear tractions, as well as fluctuations in the fragmentation depth as the compositional heterogeneities are advected through fragmentation front. We refer to these processes as unsteady fragmentation. We also demonstrate that fluctuations in the seismic force from these variations in magma composition could be a potential source of volcanic eruption tremor.

Petrological evidence suggests that compositional heterogeneities exist and evolve over the course of an eruption. A notable example is the Bishop Tuff in Long Valley, California. The Bishop Tuff formed from one of the world's largest eruptions, erupting from the Long Valley caldera over the course of 6 days at 750 ka (Hildreth & Wilson, 2007). Analysis of compositional data suggests a gradual increase in the crystal content of erupted magma as the eruption progressed, ranging from 1 to 25 wt% (Hildreth & Wilson, 2007; Gualda et al., 2004). Within a unit (i.e., eruption stage), samples exhibit fairly large ranges of crystal contents and crystal size distributions, suggesting small-scale (cm to m) heterogeneities within the same bulk composition (Pamukcu & Gualda, 2010; Pamukcu et al., 2012; Gualda & Rivers, 2006). However, compositional analysis also suggests that there were multiple bulk magma compositions due to the presence of banding and clasts of differing compositions throughout the eruption, either from pre-eruptive mixing of a vertically stratified magma body or the presence of multiple horizontally-distributed magma bodies (Hildreth & Wilson, 2007; Gualda et al., 2004; Gualda & Ghiorso, 2013). Evidence of multiple crystal populations and size distributions has been observed elsewhere, such as at Lassen Peak, California (Salisbury et al., 2008; Tepley III et al., 1999). Other proposed mechanisms of variations in crystal content throughout a magma body include

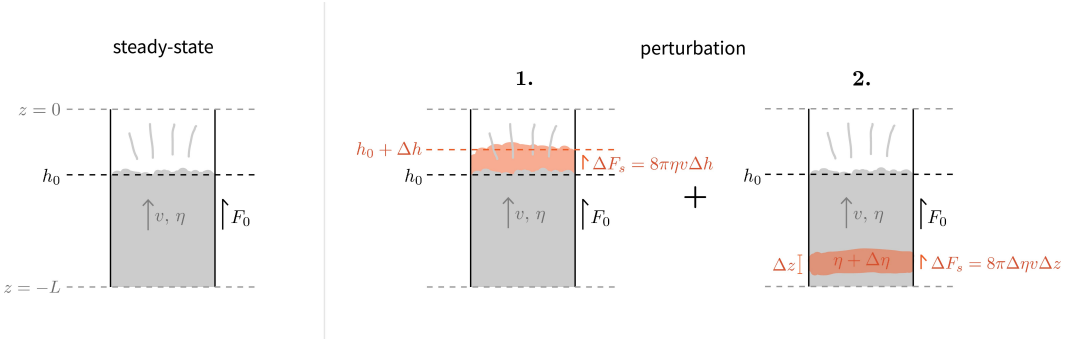

Figure 1. Schematic breaking down contributions to the seismic force from fluctuating fragmentation. Left panel shows the reference solution for a steady state eruption of magma with viscosity η flowing with constant velocity v and fragmenting at depth h_0. Second panel shows solution some short time later with changes relative to reference state indicated in red. Changes indicated represent contributions to seismic force variations arising from 1) variations in fragmentation depth and 2) variations in shear stress.

processes by which denser crystals settle toward the bottom of the magma chamber, leaving eruptable melt near the top (Hildreth & Wilson, 2007; Bachmann & Huber, 2019), e.g., melt segregation, fractional crystallization, and distillation. This could then be complexified by convective mixing of the stratified magma.

In this work, we explore how different types of compositional heterogeneity are expressed in observable seismic wave radiation. We calculate synthetic seismograms using simulation results from conduit flow modeling that captures the advection of heterogeneous magma through the conduit. We use an unsteady conduit flow model to simulate a sustained eruption with injection of heterogeneous magma through the bottom of the conduit. To simulate the viscosity variations associated with heterogeneous magma, we vary the crystal volume fraction. We investigate various injection profiles using the workflow from Coppess et al. (2022) to quantify the relation between the injection process (i.e., the timescales and amplitude of the compositional variations) and seismic wave radiation.

2 Force breakdown of unsteady fragmentation

We are interested in quantifying the seismic force fluctuations arising from unsteady fragmentation. Both quasi-static and far-field particle velocities in an elastic solid are proportional to force rate and decay as the inverse of distance, which means that unsteady fragmentation is potentially observable at both near-source and far-field stations. There may also be fluctuations in seismic moment from changes in conduit pressure, but as we will later demonstrate, the force fluctuations are almost always dominant. To start, we consider the seismic force for a general case and then take the time derivative to derive two contributions to the force fluctuations.

According to the traction-based representation presented in Coppess et al. (2022) (their Section 3), the seismic force depends on changes in shear traction acting along the conduit and chamber walls. The largest contribution to the seismic force arises from just below the fragmentation depth for several reasons. First, fragmentation is the transition from a liquid-continuous regime with high viscosity and drag to a gas-continuous regime with negligible drag. This creates an imbalance of forces as melt breaks apart and leads to a driving force that accelerates the melt upward, around and above the fragmenta-

tion depth. The velocity of the liquid-continuous, high viscosity magma is greatest at this transition point, leading to high upward shear stress. The second reason is due to the melt viscosity increasing as the dissolved volatile concentration decreases. As magma moves up the conduit, it depressurizes and volatiles exsolve from the melt, forming bubbles and increasing the melt viscosity (Hess & Dingwell, 1996). Fragmentation occurs as the increasing strain rates in the magma drive it from viscous to brittle deformation, ultimately leading to fracture of the bubble walls and linkage of the gas bubbles. The highest viscosities therefore occur just below fragmentation.

Consider the schematic of an eruption shown in Figure 1. The top of the cylindrical, vertical conduit is at $z = 0$, with the depth z being positive upward, and the fragmentation depth is $z = h(t) < 0$, which may vary in time. Below fragmentation, the wall shear stress (or drag) τ is given by the laminar flow expression

$$\tau = \frac{4\eta v}{R}, \tag{1}$$

where η is the magma viscosity, v is the cross-sectionally averaged vertical particle velocity, and R is the conduit radius. When vertically integrating the seismic force contributions over depth, we assume that contributions from drag above fragmentation are negligible, so the seismic force is

$$F_s(t) = \int_{-L}^{h(t)} 2\pi R\tau(z,t)dz, \tag{2}$$

where $-L$ is the position of the bottom boundary of the integrated region which does not vary in time. We take the time derivative of (2) and apply Leibniz's rule:

$$\dot{F}_s(t) = 2\pi R\left[\tau(h(t),t)\dot{h}(t) + \int_{-L}^{h(t)} \dot{\tau}(z,t)dz\right]. \tag{3}$$

Each term in (3) highlights one contribution to force fluctuations: the first corresponds to the fluctuating fragmentation depth with fixed shear stress and the second to variations in shear stress with fixed fragmentation depth.

We can further understand how these might change the seismic force by considering each individually and looking at perturbations around some initial state. A fluctuating fragmentation depth changes the contact area between the highly viscous magma and the conduit walls, as shown in Figure 1. If the fragmentation depth varies by some amount Δh, then the force fluctuation will be proportional to the depth change: $\Delta F_s = 8\pi\eta v\Delta h$. This is consistent with what was observed with the numerical effect in Coppess et al. (2022): the fragmentation depth dropped suddenly, leading to a downward impulse in the seismic force. Next consider the other source of force fluctations arising from variations in shear stress. Assume that the particle velocity is spatially uniform, such that any changes in shear stress arise from changes in viscosity. Suppose that a parcel of magma with viscosity $\eta+\Delta\eta$ and depth extent Δz is injected into the conduit (and is advected upward at the constant velocity). The additional force contribution from this parcel is $\Delta F_s = 8\pi\Delta\eta\, v\Delta z$, which depends on both the extent of the parcel and the difference in viscosity. This additional force will exist from the time the parcel enters the conduit until it passes through fragmentation, when it will abruptly vanish. Seismic force fluctuations in an eruption will be a combination of both of these effects, due to the relation between viscosity perturbations and fragmentation depth fluctuation dynamics. There may also be changes in velocity that arise from magma compressibility and interaction with a magma chamber held at relatively constant pressure through this process.

Breaking down the unsteady fragmentation force mechanism in this way allows us to make estimates of force fluctuations that cause seismic wave radiation. Consider representative values for magma viscosity $\eta = 5\times10^6$ Pa s and velocity $v = 2$ m/s below

fragmentation, which are consistent with the example simulation in Coppess et al. (2022) (their section 6). This magma viscosity is representative of intermediate magma compositions, like andesites and dacites that commonly occur in arc volcanoes. This is consistent with our focus on sub-Plinian style eruptions, which have been observed at arc volcanoes. In the example simulation, the fragmentation depth drops about 4 m at a time. According to the fluctuating fragmentation depth contribution estimate, this yields a downward force change of $\sim 10^9$ N, which is consistent with the amplitude of the sharp force change in Coppess et al. (2022). The duration of the force change is determined by the rate of fragmentation depth variations. In the numerical intermittent descent example, the depth drops instantaneously and leads to the very sharp feature observed. Force changes of 10^9 N yield seismic amplitudes on the order of ~ 10 μm/s for stations located a few kilometers from the vent (Coppess et al., 2022). These amplitudes are generally observable.

Next we construct an example case for the viscosity variation contribution, using the same representative values for magma viscosity and velocity just below fragmentation. Consider a parcel of magma with thickness $\Delta z = 10$ m and higher viscosity $\Delta\eta = 10^6$ Pa s. The associated force change is $5{\times}10^8$ N, which yields comparable seismic amplitudes to the intermittent descent contribution. Since the largest force fluctuations arise just below fragmentation, the duration of the signal will be determined by how quickly the parcel is advected through the fragmentation front, which is approximately $\Delta z/v = 5$ s ($\sim$0.2 Hz). If the parcel were smaller, then the force change would be of smaller amplitude and higher frequency.

Overall these estimates establish the feasibility of observable seismic wave radiation from fluctuations in the fragmentation process. Next we utilize unsteady conduit flow simulations to investigate this problem in more detail.

3 Methodology

To simulate the conduit flow response to heterogeneities in magma composition, we investigate the conduit flow dynamics that arise from perturbations around steady-state eruption conditions. Starting with initial conditions representing an ongoing steady eruption, we vary the magma composition flowing into the conduit and simulate the system response using an unsteady conduit flow model. We use the simulation results to calculate synthetic seismograms using the workflow presented in Coppess et al. (2022) (summarized in their Section 2) to demonstrate how the seismic signal connects to the internal fluid dynamics.

Our unsteady conduit flow model solves for quasi-1D adiabatic flow of multiphase fluid (exsolved water, liquid melt, dissolved water, and crystals). For the rest of this study, we use the term "magma" to refer to the combination of the following phases: liquid melt, dissolved water, and crystals. All phases are assumed to share a common temperature, pressure and particle velocity. Gas exsolution from the melt occurs over a specified timescale, and we account for the dependence of magma viscosity on temperature, dissolved volatile content and crystal content using experimentally constrained empirical relations. We assume a linear viscous rheology for the magma for simplicity. Fragmentation is captured through a smoothed drop of the wall shear stress to zero, marking the transition to a low-viscosity and turbulent gas-continuous regime in the upper conduit above fragmentation. Since turbulent drag is many orders of magnitude smaller than the drag below fragmentation, we neglect its contribution to the wall shear stress and seismic force.

To help visualize fragmentation, we define an effective viscosity as the product of the magma viscosity and the volume fraction of unfragmented magma. Therefore the effective viscosity is identical to the magma viscosity below fragmentation and drops to zero as the magma fragments. We use this effective viscosity in the plots to follow. The

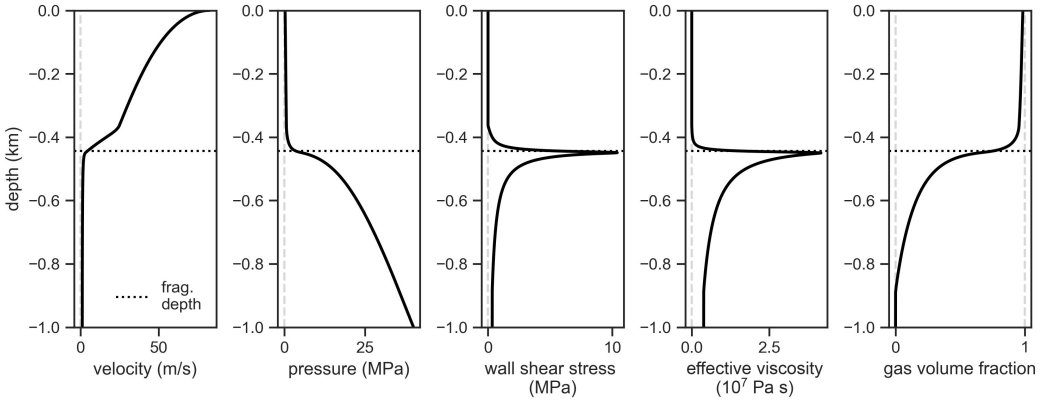

Figure 2. Initial steady state solution. Parameter values are given in Table 1. Fragmentation occurs when the gas volume fraction exceeds 0.75. Effective viscosity is the product of the magma viscosity and the volume fraction of unfragmented magma (see text).

smoothed transition in wall shear stress represents the finite timescale of the fragmentation process. This timescale is a model parameter that can be chosen to correspond with the relevant timescale of a proposed fragmentation mechanism. It also serves to introduce (together with the magma ascent velocity) a length scale that must be resolved in the spatial discretization of the governing equations. In this model, we adopt a critical gas volume fraction fragmentation condition for simplicity: when the exsolved gas volume fraction exceeds this threshold, the magma is considered fragmented and the wall shear stress is reduced toward zero. Utilizing a fragmentation criterion based on a critical gas overpressure or strain rate would be more realistic (Papale, 1999; Gonnermann & Manga, 2003; Melnik & Sparks, 2002; Scheu & Dingwell, 2022), but is left for future work. For more specifics of the conduit flow model used in this study, we refer the reader to Appendix A.

3.1 Steady-state solution

To initialize the simulation, we choose a steady-state solution defined by a bottom pressure boundary condition and choked flow through the vent. While we do not model the eruptive jet and plume, the model provides the time-dependent mass eruption rate, which can be used in a model of the eruptive jet and plume to allow comparison with observations. The crystal volume fraction ϕ_c (volume of crystals / volume of magma) is constant with depth. See Appendix B for details on the relevant considerations that went into choosing the solution used to initialize the simulations.

The chosen solution is shown in Figure 2. Magma is injected at the bottom boundary at a pressure of 40 MPa, corresponding to an inlet velocity of $\sim$1 m/s. As the magma moves up through the conduit, drag and the reduced weight of the overlying magma column leads to depressurization of magma. Eventually, the melt becomes supersaturated with volatiles and exsolution starts when it reaches a depth of 900 m. As exsolution progresses and the gas volume fraction increases, the viscosity of the melt begins to increase as the dissolved volatile content drops. This leads to progressively increasing drag along the conduit walls (as velocity is not changing significantly), which leads to an increased pressure gradient. At around a depth of 450 m, the gas volume fraction reaches the critical threshold for fragmentation to occur; the magma viscosity reaches its peak just below this depth. Fragmentation is accompanied by a reduction in drag. Above the frag-

Table 1. Parameter values used in steady-state solution in Section 3.1.

Symbol	Description	Numerical value
g	gravitational acceleration	9.8 m/s^2
$\overline{\phi}_0$	critical gas volume fraction	0.75
t_{ex}	exsolution timescale	10 s
t_f	fragmentation timescale	1 s
ζ	fragmentation smoothing scale	0.15
S_m	solubility constant	5×10^{-6} Pa$^{1/2}$
χ_0	water mass concentration at base of conduit	0.03
ϕ_{c0}	bulk crystal volume fraction	0.4
R_G	specific gas constant	461 J/(kg K)
T_{ch}	chamber temperature	1050 K
p_{ch}	chamber pressure	40 MPa
K	magma bulk modulus	10^9 Pa
$\rho_{\text{mag},0}$	reference magma density	2600 kg/m^3
p_0	reference pressure	χ_0^2/S_m^2
$C_{\text{v,ex}}$	exsolved water heat capacity	1827 J/(kg K)
$C_{\text{v,mag}}$	magma heat capacity	3000 J/(kg K)
R	conduit radius	50 m
L	conduit length	1 km
ρ_r	rock density	2700 kg/m^3
c_p	P-wave speed	3.464 km/s
c_s	S-wave speed	2 km/s

mentation depth, the wall shear stress drops toward zero and the magma is accelerated upward.

3.2 Injection profiles of heterogeneous magma

In this section we explain how heterogeneities in magma are introduced through the bottom boundary of the conduit flow model. These heterogeneities are then advected upward through the conduit and lead to unsteady perturbations of the fragmentation front. In concept, the steady state solution could be unstable to perturbations. However, we see no evidence for this for the parameter space explored in this study. We also explain how we parametrize the magma heterogeneities by specifying variations in crystal content and how this affects magma viscosity.

The inlet pressure at the bottom boundary remains constant throughout the simulation. We specify the composition of magma by setting the partial densities of each phase at the boundary (i.e., the mass of some phase relative to the total volume, denoted as $\overline{\rho}$ with a subscript identifying the phase: *ex* for exsolved water, *dis* for dissolved water, *w* for total water, *c* for crystals, *melt* for melt, and *mag* for magma). For our selected parameters, the exsolution depth is contained within the simulated domain, so no exsolved water enters the conduit (i.e., $\overline{\rho}_{\text{ex}} = 0$). This means that magma partial density is the same as magma phasic density and total mixture density ($\overline{\rho}_{\text{mag}} = \rho$), which allows us to use the magma equation of state with the inlet pressure to define the magma partial density. It also means that the total water partial density is equal to the dissolved water partial density: $\overline{\rho}_{\text{w}} = \overline{\rho}_{\text{dis}}$.

To clarify the relation between magma composition variations and viscosity variations, we assume that the injected dissolved water mass concentration χ_0 (mass of dissolved water / mass of melt) remains constant. This means that only variations in crys-

tal volume fraction ϕ_c (volume of crystals / volume of magma) contribute to viscosity perturbations. This is done to simplify specification of the boundary conditions. To summarize, the conditions used to specify the magma composition at the bottom boundary are as follows:

$$\overline{\rho}_{\mathrm{ex}} = 0, \tag{4}$$

$$\overline{\rho}_{\mathrm{dis}}/\overline{\rho}_{\mathrm{melt}} = \chi_0, \tag{5}$$

$$\overline{\rho}_c/\overline{\rho}_{\mathrm{mag}} = \phi_c(t), \tag{6}$$

$$\overline{\rho}_{\mathrm{mag}} = \overline{\rho}_{\mathrm{melt}} + \overline{\rho}_{\mathrm{dis}} + \overline{\rho}_c = \rho(p_{\mathrm{bot}}) \tag{7}$$

where p_{bot} is the chamber pressure and $\phi_c(t)$ defines some time-dependent variation in crystal volume fraction, which we will specify later to represent different injection profiles. In addition, since there is no exsolved water at the bottom boundary, the mixture density $\rho(p)$ is defined using a linearized equation of state for magma:

$$\rho(p) = \rho_{\mathrm{mag}} = \rho_{\mathrm{mag},0}\left(1 + \frac{p - p_0}{K}\right), \tag{8}$$

where $\rho_{\mathrm{mag},0}$, p_0, and K are the reference density, reference pressure, and bulk modulus for magma. We rearrange these expressions to find an equivalent definition of the partial densities of the different components, representing what is actually specified in the code:

$$\overline{\rho}_{\mathrm{ex}} = 0, \tag{9}$$

$$\overline{\rho}_{\mathrm{mag}} = \rho(p_{\mathrm{bot}}), \tag{10}$$

$$\overline{\rho}_c = \phi_c(t)\rho(p_{\mathrm{bot}}), \tag{11}$$

$$\overline{\rho}_{\mathrm{w}} = \chi_0\left(\frac{\overline{\rho}_{\mathrm{mag}} - \overline{\rho}_c}{1 + \chi_0}\right) = \frac{\chi_0(1 - \phi_c(t))}{1 + \chi_0}\rho(p_{\mathrm{bot}}). \tag{12}$$

To systematically understand the relation between magma heterogeneity profiles and the resulting seismic radiation, we consider a sequence of increasingly complex injection profiles. At the bottom boundary, the injected crystal volume fraction is defined as:

$$\phi_c(t) = \phi_{c0} + \delta\phi_c(t) \tag{13}$$

where ϕ_{c0} is the reference bulk crystal volume fraction and $\delta\phi_c(t)$ is the fluctuation about that reference value.

The first injection profile we consider is that of a Gaussian pulse of higher crystal volume fraction:

$$\delta\phi_c(t) = Ae^{-(t-t_p)^2/(2\sigma^2)}, \tag{14}$$

where A is the amplitude of the pulse, t_p is the time where the peak occurs, and σ is the width of the pulse. This represents the advection of a magma parcel of differing composition. This also serves as a simple case to understand the feedback mechanisms and forces at play and how those translate into the seismic radiation. We consider two example pulses of same amplitude ($A = 0.1$) but different widths ($\sigma = 16$ s, $t_p = 60$ s; and $\sigma = 8$ s, $t_p = 40$ s).

We build upon this example to increasingly complex and ultimately stochastic heterogeneity injections. It is reasonable to presume that stochastic variations in magma composition would yield stochastic variations in the fragmentation depth, which would be reflected in the associated, incoherent seismic radiation. Before jumping to a fully stochastic injection scheme, we first inject sinusoidal profiles of different frequencies:

$$\delta\phi_c(t) = A\sin(2\pi ft), \tag{15}$$

where f is the frequency of crystal content oscillations. Due to numerical limits on spatial resolution, the maximum frequency of injection that we can simulate is ~ 0.25 Hz. We consider three different frequencies (all with $A = 0.1\phi_{c0}$): 0.0625 Hz, 0.125 Hz, and 0.25 Hz.

For modeling stochastic heterogeneity, $\delta\phi_c(t)$ is a stationary Gaussian random function with zero mean and exponential autocorrelation. The autocorrelation function is

$$R_c(t) = \langle \delta\phi_c(\gamma)\delta\phi_c(\gamma + t)\rangle = \varepsilon^2 e^{-|t|/t_{\text{cor}}} \tag{16}$$

where $\langle\cdot\rangle$ denotes an ensemble average, ε is the standard deviation of the fluctuations, and t_{cor} is the correlation timescale. This correlation timescale can be connected to a correlation length scale within the magma body supplying the conduit by multiplying t_{cor} by the inlet velocity v_{in}. Taking the Fourier transform of the autocorrelation function gives us the two-sided power spectral density (PSD) function:

$$P_c(\omega) = \frac{2\varepsilon^2 t_{\text{cor}}}{1 + \omega^2 t_{\text{cor}}^2}, \tag{17}$$

where ω is angular frequency. We respect the spatial resolution constraints of the numerical method by bounding the allowed wavelengths in the power spectral density of the crystal volume fraction variation (by setting the spectral amplitudes to zero above the maximum resolvable frequency, 0.25 Hz). We consider two stochastic profiles with the same standard deviation ($\varepsilon = 0.03$) but different correlation timescales ($t_{\text{cor}} = 1$ s, 10 s).

3.3 Seismic force and moment and synthetic seismograms

We calculate synthetic seismograms using the point source workflow in Coppess et al. (2022) for a cylindrical conduit oriented along the z-axis. First, the results from the conduit flow simulations are translated into equivalent force and moment histories by calculating changes in tractions and pressure relative to the initial pre-stressed state (in this case the steady-state eruption solution used to initialize all simulations). Changes in shear traction $\Delta\tau(z,t)$ are integrated over the walls of the conduit, defining the seismic force as follows:

$$F_i(t) = \delta_{iz} 2\pi R \int_{z_{\text{bot}}}^{0} \Delta\tau(z,t)dz, \tag{18}$$

where z_{bot} is the depth of the bottom conduit boundary and the conduit vent is at $z = 0$. Similarly, we depth-integrate pressure changes $\Delta p(z,t)$ to define the associated moment tensor history for a cylindrical pipe geometry:

$$M_{ij}(t) = \left[(\lambda + 2\mu)\delta_{ij} - 2\mu\delta_{iz}\delta_{jz}\right] \frac{A}{\mu} \int_{z_{\text{bot}}}^{0} \Delta p(z,t)dz, \tag{19}$$

where λ is the first Lamé parameter and μ is shear modulus. Force and moment histories are then convolved with the Green's function of the elastic wave equation to calculated the synthetic seismograms. We compute the Green's functions using the FK method implemented by Zhu and Rivera (2002) for a homogeneous half-space with density 2700 kg/m^3, P-wave speed 3.464 km/s, and S-wave speed 2 km/s. The Green's functions are calculated for a source depth of 500 m (i.e., mid-way through the conduit) and a station placed on the surface, 10 km from the vent. The relative dimensions of the conduit and station distance justifies the use of the point source representation to calculate the associated seismic radiation. Finally, we do not include tilt contributions to the radial seismograms, which are likely to be important in the ULP and possibly VLP frequency bands.

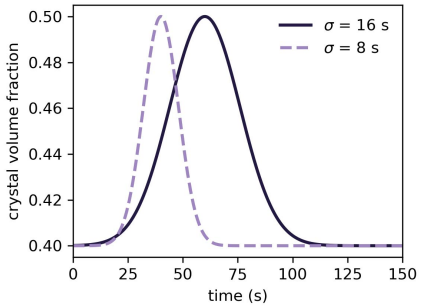

Figure 3. Gaussian pulse crystal volume fraction injection profiles.

4 Results

4.1 Gaussian pulse

Magma enters the conduit at constant pressure and initially ascends as a relatively incompressible fluid at nearly constant velocity. The Gaussian pulse (Figure 3) is a parcel of magma with higher crystallinity, higher viscosity, and higher drag than the rest of the magma. Therefore, a larger pressure gradient is required to push the parcel through the conduit. This reduces the pressure in the conduit at and above the parcel (Figures 4 and 5), enhances gas exsolution, and causes the exsolution and fragmentation depths to descend (Figure 6). They eventually return to their initial depths after the parcel is fully fragmented.

The region of highest viscosity and wall shear stress just below the fragmentation depth descends as fragmentation descends in the conduit. Therefore, the wall shear stress decreases around the initial fragmentation depth and increases below it, explaining the pattern in wall shear stress change seen in Figures 4 and 5. The depth integral of this change is proportional to the seismic force. We note that despite a partial cancellation of the positive and negative changes in wall shear stress, the net force increases as the parcel ascends through the conduit and passes through fragmentation because of the higher drag associated with the crystal-rich parcel.

As the parcel passes through fragmentation, the velocity decreases, not only around fragmentation but also in the upper section of the conduit. The mass eruption rate drops by about 50%. Interestingly, despite the Gaussian pulse width being only about $2\sigma = 32$ s, the reduction in mass eruption rate lasts for more than one minute. A similar increase in duration is seen for the crystal volume fraction. This is explained by the time-varying fragmentation depth, which alters the particle velocity distribution and hence particle paths within the conduit. Magma at the leading edge of the Gaussian pulse fragments lower in the conduit and then quickly ascends to the vent. In contrast, magma at the trailing edge of the pulse fragments higher in the conduit, and thus spends more time at the slower velocities characteristic of the unfragmented magma. This broadens the pulse duration and its expression in the time history of crystal content through the vent and the mass eruption rate.

Many of these processes are reflected in the seismic force and moment histories (Figure 10). When the pulse enters the conduit and ascends, the associated depressurization of the upper conduit is captured in the progressive decrease in the seismic moment. The seismic force also progressively increases (in the upward direction) due to the higher viscosity and drag of the parcel, which increase as gas exsolves. The fragmentation front is descending through the conduit during this period (Figure 6), dropping about 20 m

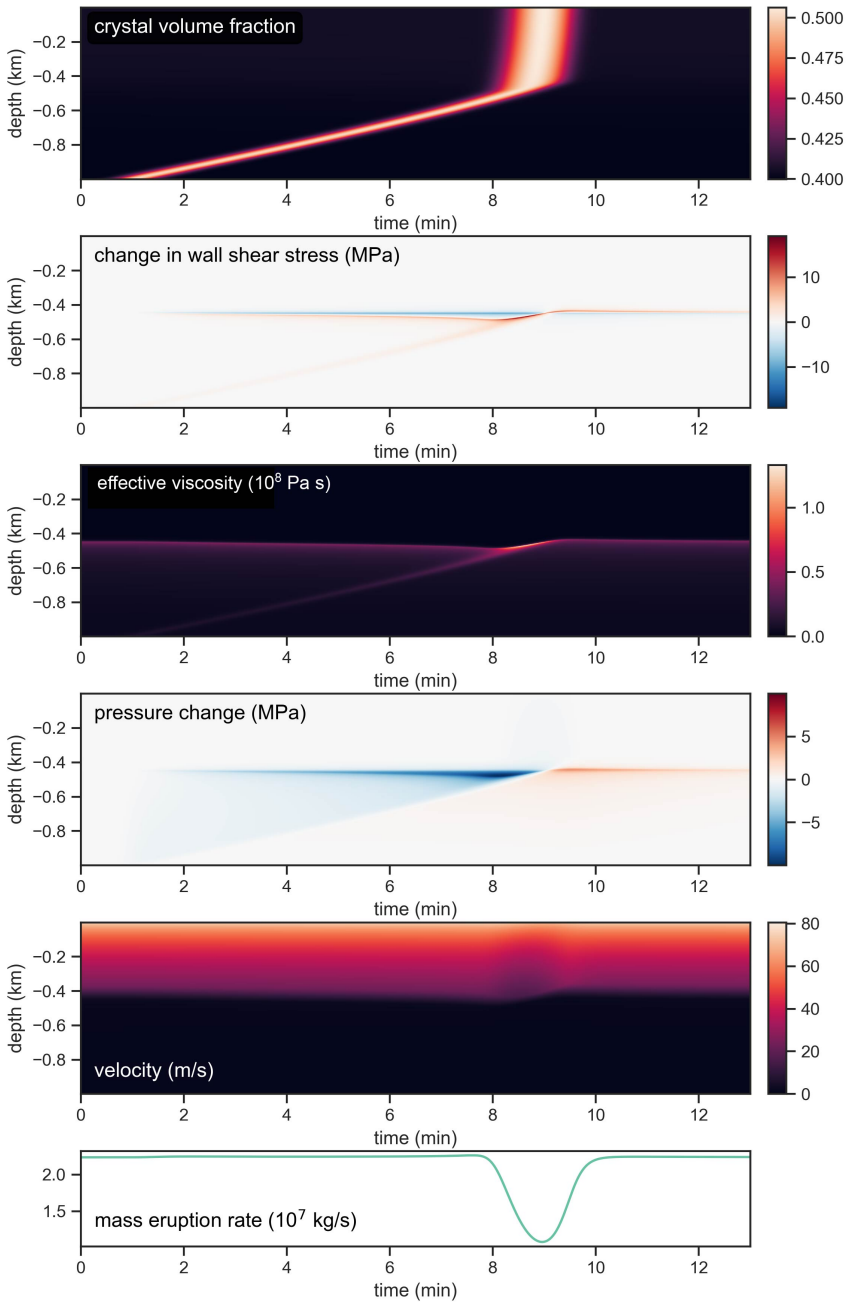

Figure 4. Gaussian pulse simulation results for $\sigma = 16$ s.

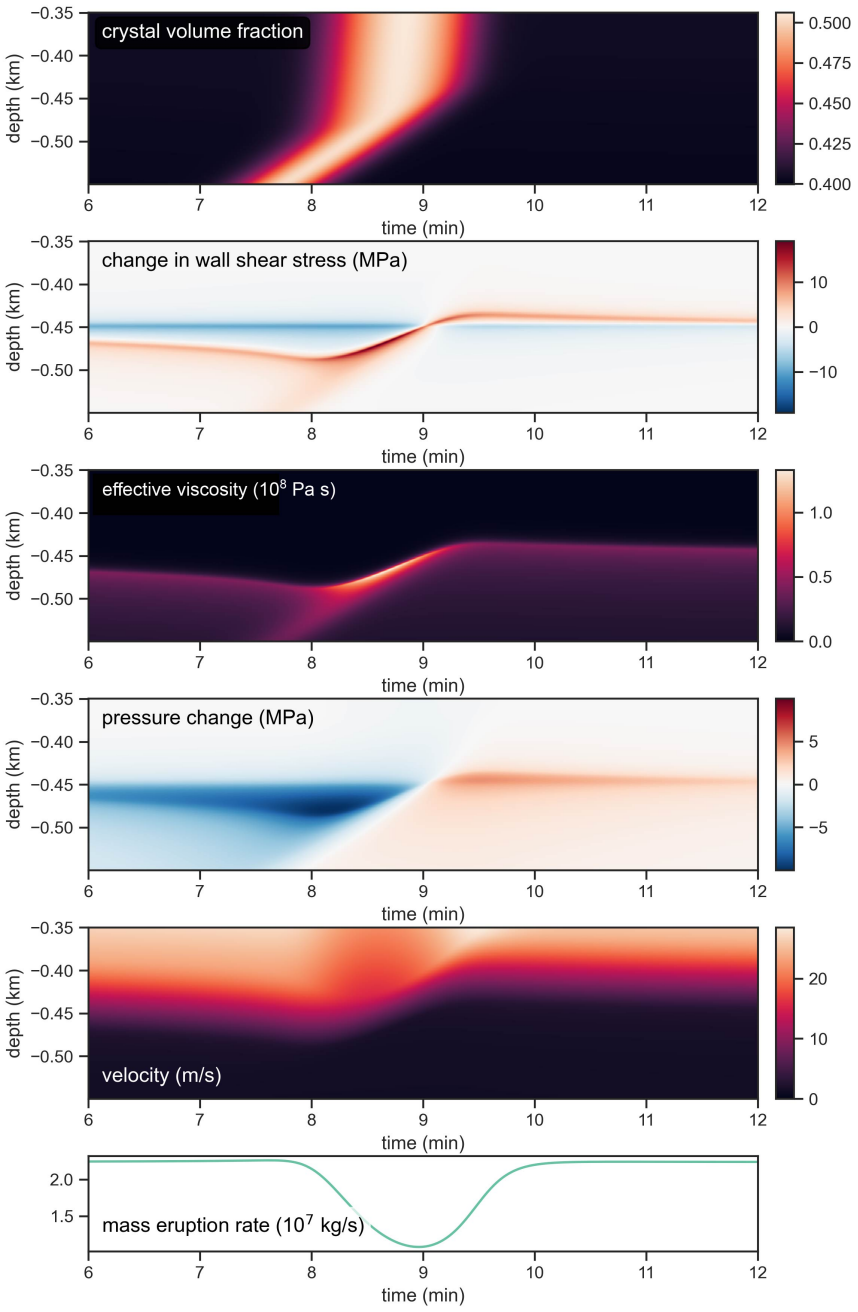

Figure 5. Zoomed in version of Figure 4 for Gaussian pulse with $\sigma = 16$ s.

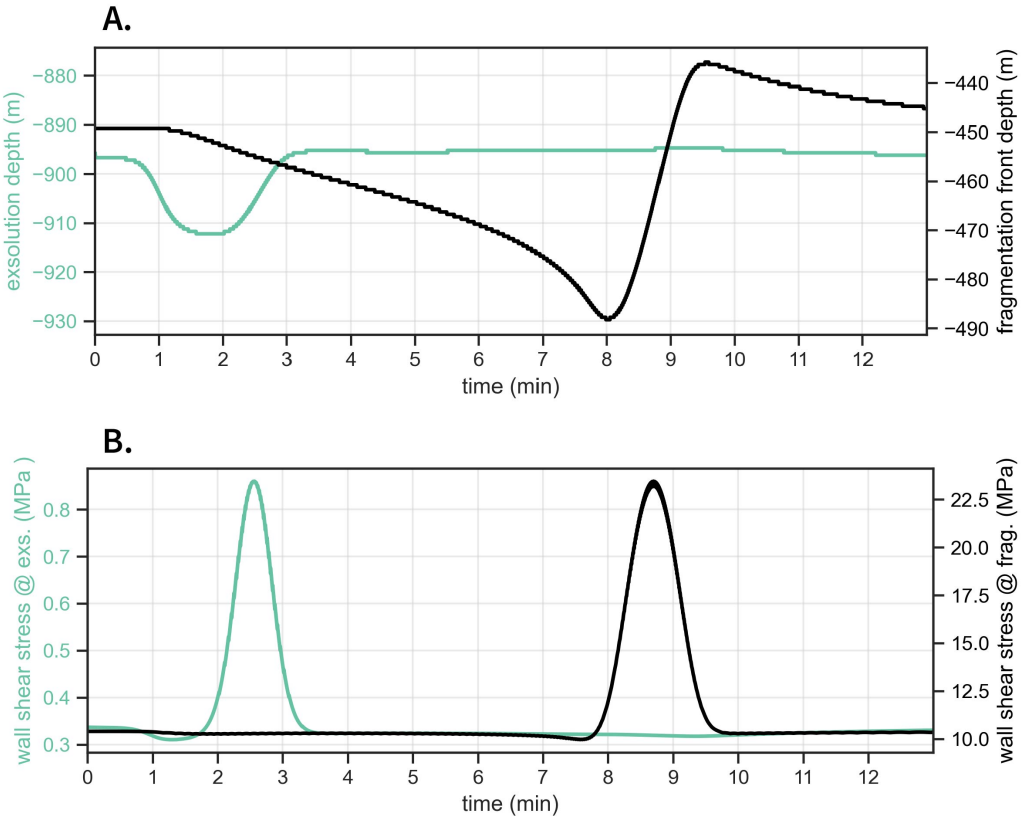

Figure 6. Fragmentation and exsolution depth evolution with time for injection of Gaussian pulse with $\sigma = 16$ s: **A.** Fragmentation and exsolution depths. **B.** Wall shear stress at fragmentation and exsolution depths.

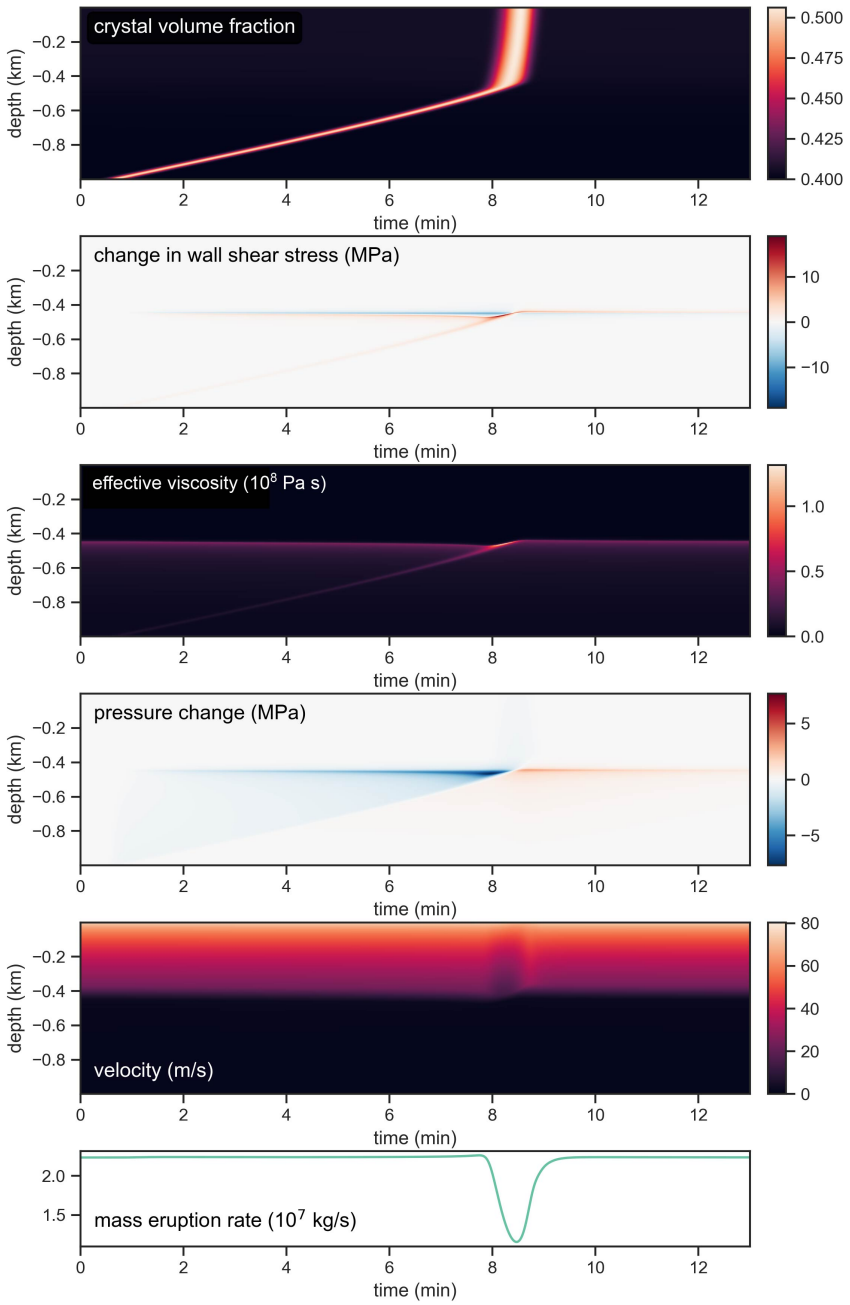

Figure 7. Gaussian pulse simulation results for $\sigma = 8$ s.

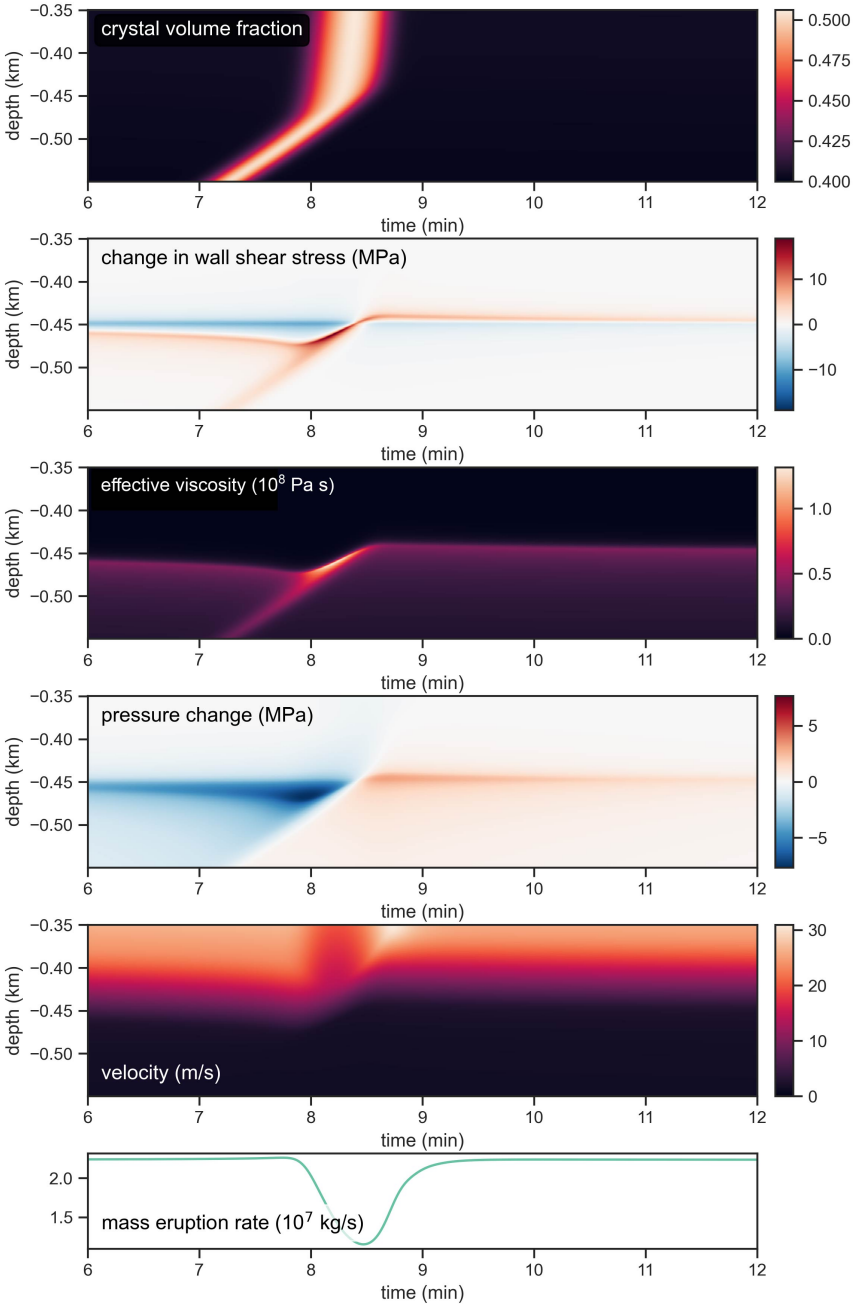

Figure 8. Zoomed in version of Figure 7 for Gaussian pulse with $\sigma = 8$ s.

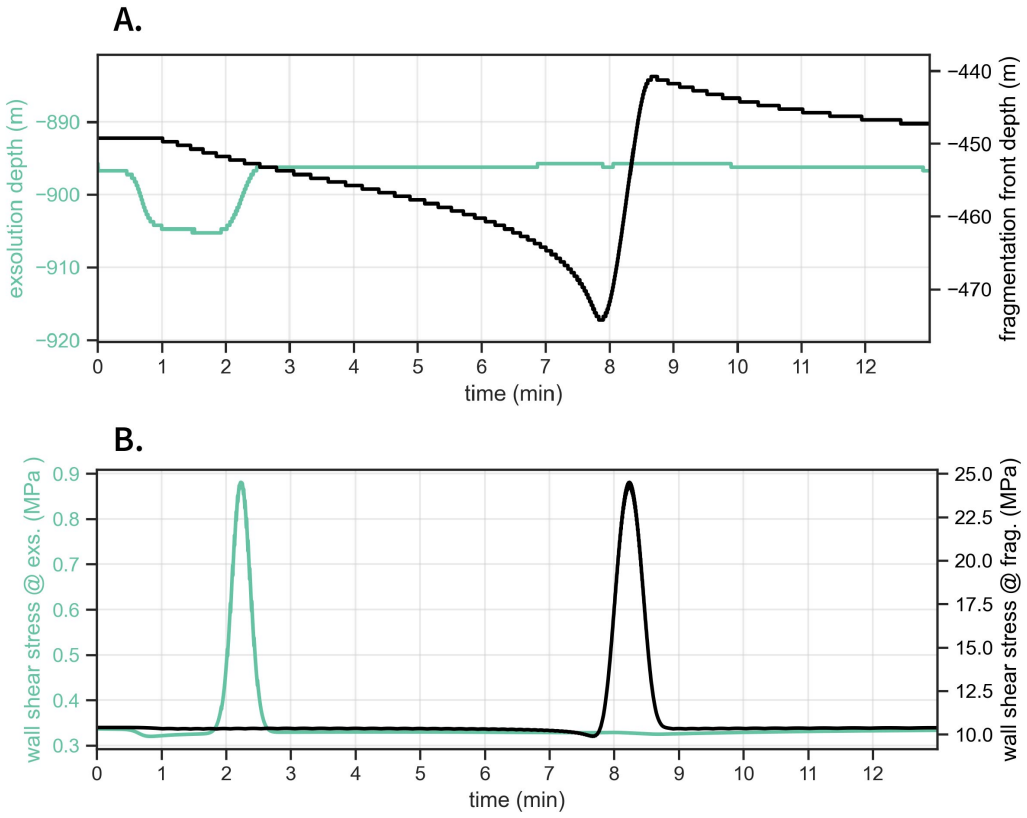

Figure 9. Fragmentation and exsolution depth evolution with time for injection of Gaussian pulse with $\sigma = 8$ s: **A.** Fragmentation and exsolution depths. **B.** Wall shear stress at fragmentation and exsolution depths.

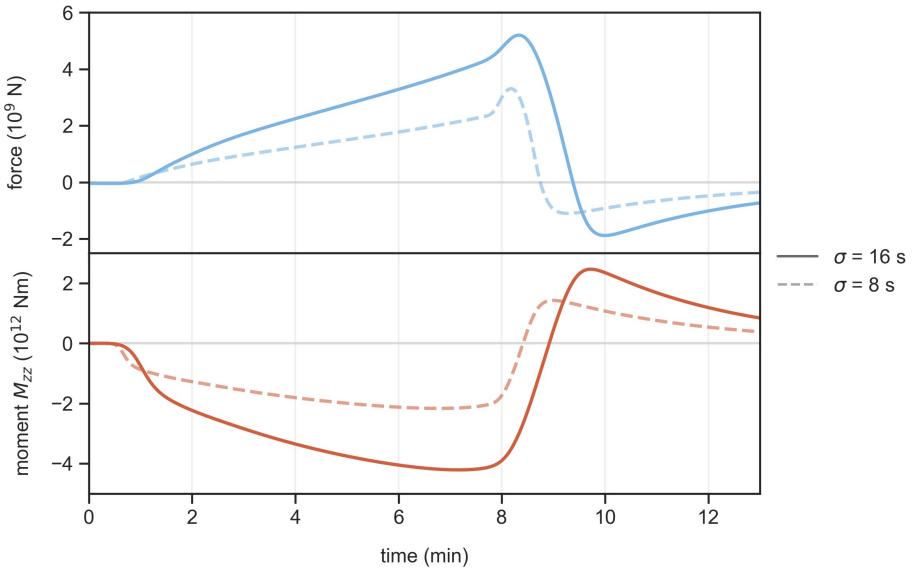

Figure 10. Seismic force and moment histories for Gaussian pulse injections. The other nonzero moment tensor components, $M_{xx} = M_{yy}$, are proportional to M_{zz}.

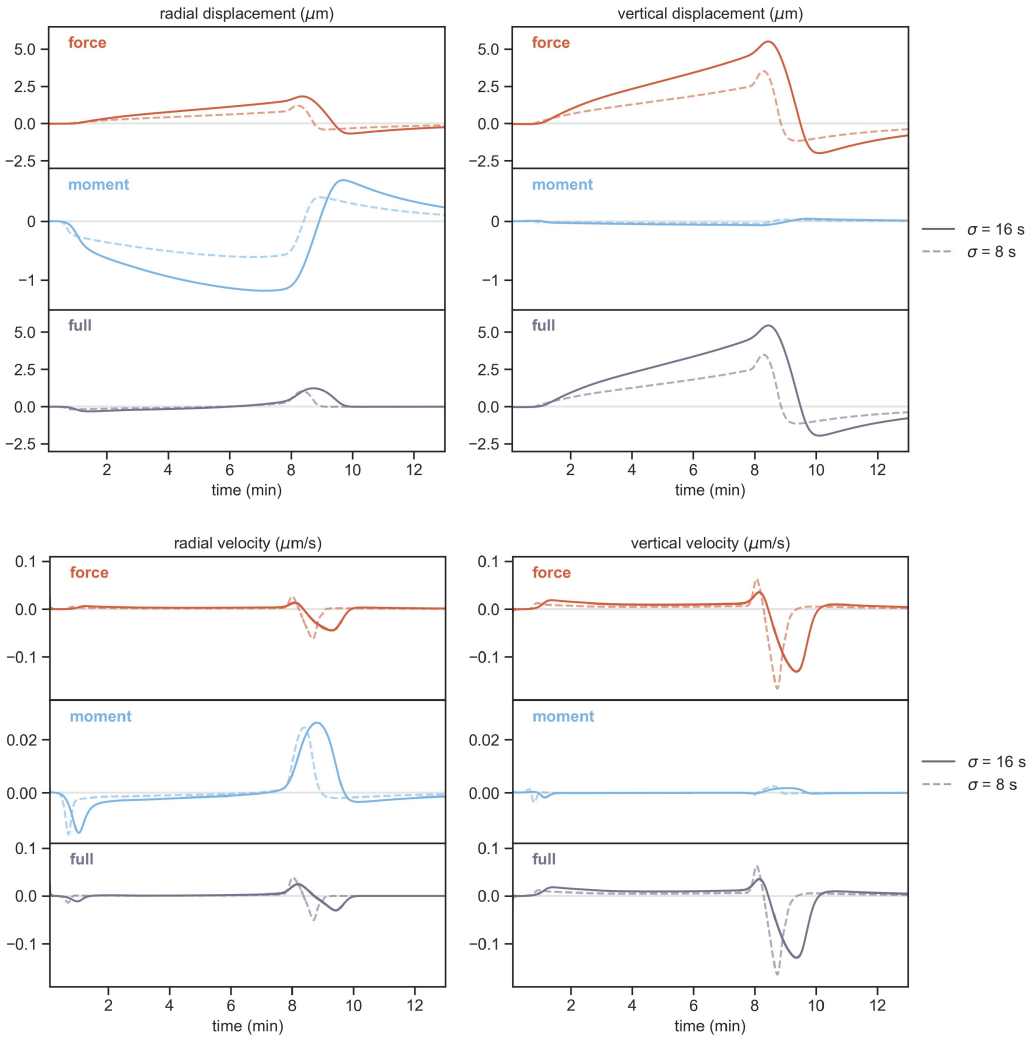

Figure 11. Synthetic displacement and velocity seismograms for Gaussian pulse injections at a receiver 10 km from vent.

over the course of 7 minutes. During this ramp-up period, the two contributions to the seismic force, introduced in Section 2, are as follows: 1) The fragmentation depth drops about 20 m with a viscosity $\sim 10^7$ Pa s, corresponding to a force fluctuation $\Delta F_s \sim -5 \times 10^9$ N. 2) The width of the pulse is about 40 m with a viscosity difference on the order of 10^7 Pa s, corresponding to expected $\Delta F_s \sim 10^{10}$ N. These two combinations are the same order of magnitude but have opposite sign. This is confirmed by the smaller force change of $\sim 10^9$ N calculated from integration over the conduit walls, indicating that the contribution from the viscosity variation is larger than that from the change in fragmentation depth.

As the parcel is being pushed through the fragmentation depth, the seismic moment increases and switches from negative to positive as overpressure develops below the parcel (Figure 10). The upward seismic force decreases and eventually switches direction. The higher pressures below the parcel slow exsolution. This leads to more water being dissolved in the melt, which decreases the viscosity. Therefore, once the parcel fragments, the viscosity over the whole conduit is less than for the initial steady-state. So even though the fragmentation front has moved upward, it has not moved a sufficient amount to counteract the decrease in force from the reduction in viscosity.

Figure 11 shows the associated synthetic displacement and velocity seismograms. The receiver is $r = 10$ km from the vent. The solid response becomes quasi-static at periods greater than $\sim$30 s, for which $\omega r/c_s < 1$ (for angular frequency ω and shear wave speed c_s). Displacements are proportional to force and moment in this limit, and particle velocities are proportional to their time derivatives. Thus displacement seismograms at these long periods are effectively a linear combination of the seismic force and moment histories, and thus capture the progression of the parcel through the conduit and eventually the fragmentation front. Force and moment contributions are comparable in the radial component of displacement but with competing effects. The vertical component is dominated by the force contribution. In the velocity seismograms – which are dominated by force contributions in all components – there is an initial signature associated with the parcel entering the conduit, followed later by a distinct VLP feature associated with the parcel passing through fragmentation and the associated reduction in upward force. The force change is therefore downward and is reflected in the downward pulse in the vertical velocity seismogram. The combination of this seismic signal with the approximately coincident reduction in mass eruption rate provides an observationally testable prediction of what occurs when high crystal content magma is fragmented. Such a significant drop in mass eruption rate would likely disrupt the eruption column, yielding observable signal in infrared or visual data, gas emission data, and possibly also in infrasound data, depending on how impulsive the process is.

The smaller width Gaussian pulse ($\sigma = 8$ s instead of 16 s in the previous example) exhibits a similar sequence of events as the wider pulse, with differences arising in the timing and amplitude of force and pressure changes (Figures 7 and 8). The smaller width means that there is less total drag provided by the parcel because the contact area between the parcel and the conduit walls is smaller. Therefore, the parcel requires less overpressure to push it through the conduit. The parcel also moves up the conduit faster, so the differential flow between the parcel and the magma above it is less than for the wider pulse. As a result, the magma above depressurizes at a slower rate in this case. This is confirmed by the reduced descent of the fragmentation front (Figure 9). The smaller parcel is also advected through fragmentation more quickly, which leads to a sharper reduction in the mass eruption rate (Figure 8) and the seismic force (Figure 10).

The associated displacement seismograms have smaller amplitude than for the wider pulse, but the velocity seismograms exhibit a higher amplitude but shorter duration feature as the parcel passes through fragmentation (Figure 11). The duration of both the mass eruption rate reduction and the VLP signatures may indicate the size of the parcel being advected through the conduit. The amplitude of the VLP feature depends on

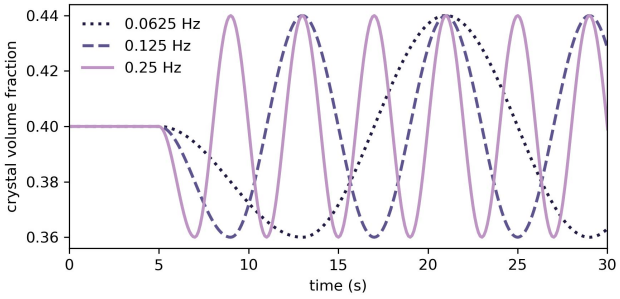

Figure 12. Sinusoidal crystal volume fraction injection profiles.

both the relative crystal content or viscosity of the parcel as well as its size. Therefore, seismic amplitude on its own may not be sufficient to make an estimation of the crystal content of the parcel. However, the amplitude of reduction in mass eruption rate is about the same for the two parcel sizes, indicating that it might serve as a diagnostic for the composition of the parcel.

4.2 Sinusoid

Next we examine simulations of the injection of a sinusoidal crystal volume fraction profile. The injection profiles are shown in Figure 12. The initial adjustment phase of the simulation, when heterogeneities ascend through the conduit and displace the homogeneous magma, is similar to the Gaussian pulse. Specifically, the net drag and viscous pressure drop increase and there is an overall increasing trend in seismic force and moment. This phase is not shown in the figures as we choose to focus instead on the fully "spun-up" state (i.e., when the solution reaches a periodic limit cycle) to highlight the higher frequency signatures associated with the advection of the composition variations through fragmentation.

We can think of the sinusoidal variations as a series of parcels with alternating higher and lower crystal content. Even though the injected crystal content varies sinusoidally, the nonlinear dependence of viscosity on crystal volume fraction leads to nonsinusoidal but periodic variations in viscosity, fragmentation depth, and other features in the solution (Figure 13). The general behavior is similar to what was seen for the Gaussian pulse simulations. The fragmentation depth decreases as high crystallinity parcels approach fragmentation. This is because the viscous pressure drop is higher, due to the higher viscosity from both the higher crystallinity and the additional exsolution that accompanies the pressure drop. As the high crystallinity parcels fragment, the fragmentation depth rises. This process is accentuated by the passage of a low crystallinity parcel through fragmentation. The oscillations in the fragmentation depth are nonsinusoidal, with rapid descent followed by more gradual rise (Figure 14).

The mass eruption rate also varies periodically. Interestingly, the maximum mass eruption rate occurs as high crystallinity magma passes through fragmentation and exits the vent. This is different from the Gaussian pulse. We suspect that the phase relations between different solution components, such as crystal content and mass eruption rate, may change as a function of frequency due to the nonlinear dynamics of the system response. A more thorough investigation may be warranted, but this is beyond the scope of our study.

The magnitude of the force fluctuations are smaller than for the Gaussian case because of the smaller amplitude of crystal content variation used – leading to lower peak

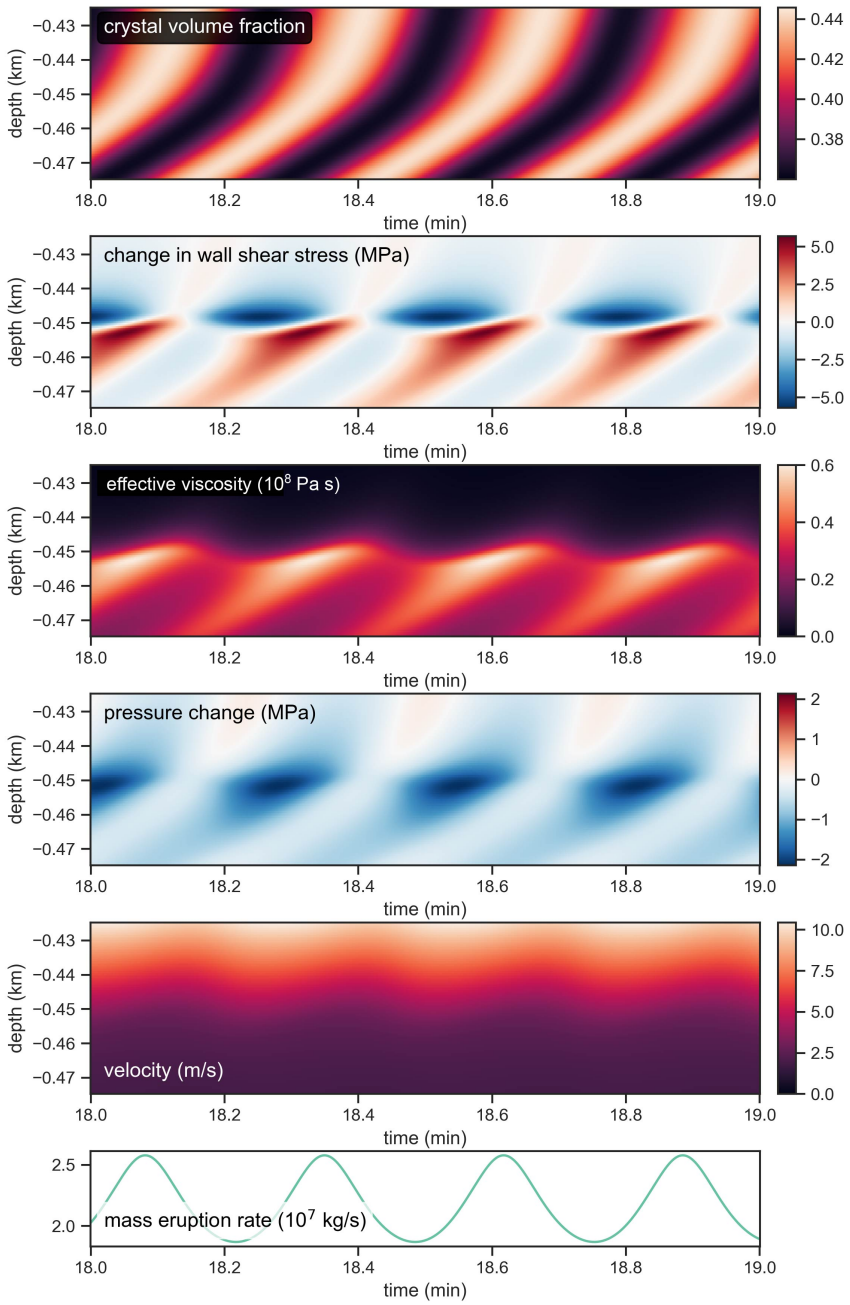

Figure 13. 0.0625 Hz sinusoidal injection simulation results.

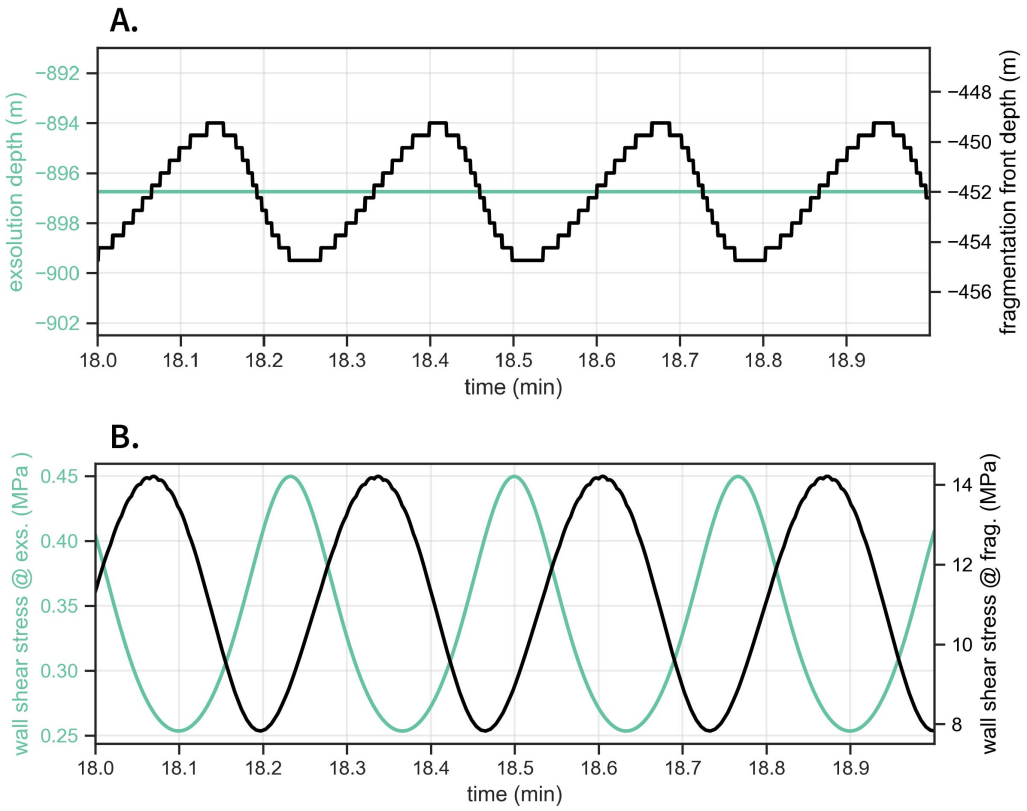

Figure 14. Fragmentation and exsolution depth evolution with time for injection of 0.0625 Hz sinusoid: **A.** Fragmentation and exsolution depths. **B.** Wall shear stress at fragmentation and exsolution depths.

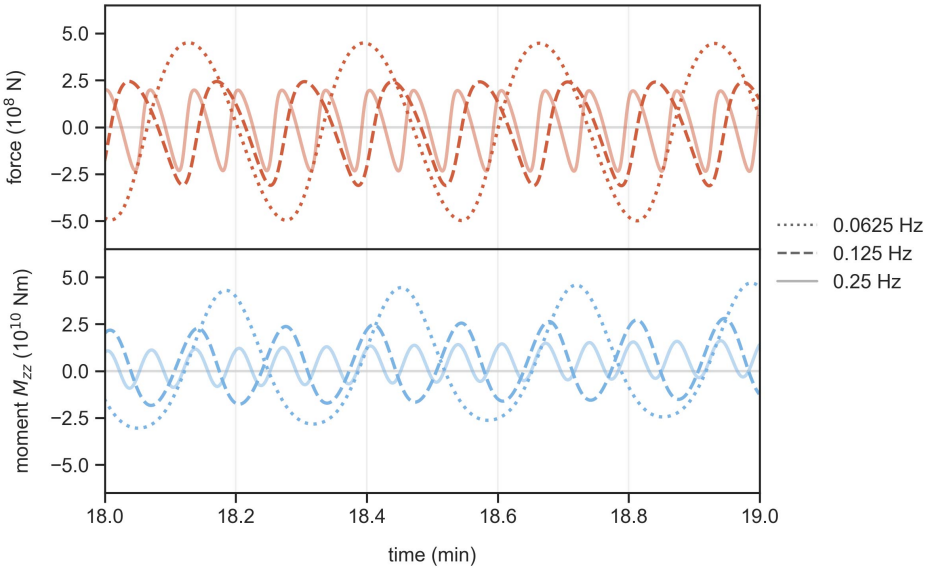

Figure 15. Seismic force and moment histories for different frequency sinusoidal injections. Force and moment histories have been de-meaned. The other nonzero moment tensor components, $M_{xx} = M_{yy}$, are proportional to M_{zz}.

viscosities – and the fragmentation depth fluctuates over a smaller range (Figure 14). The peaks of the force fluctuations correspond to the passage of a high crystallinity parcel through fragmentation, as this parcel has the largest peak viscosity and the fragmentation front moves upward. The troughs in force correspond to low crystallinity parcels passing through fragmentation, due to the lower viscosities and the fragmentation front moving back down. For the low frequency injection, the parcels are larger and take longer to fragment, which determines the frequency of the force fluctuations. Thus, the force fluctuation frequency increases with increasing injection frequency. On the other hand, the force fluctuation amplitude decreases with increasing frequency, though the relationship is nonlinear and appears to saturate (Figure 15). The largest viscosities occur within high crystallinity parcels that have just reached fragmentation. The value of the peak viscosity is the same across all frequency injections because that is determined by the peak crystal volume fraction (which is the same) and the amount of dissolved gas (which is also approximately the same). However, the contact area between the high crystallinity parcels and the conduit walls is different, as the different frequencies yield different spatial extents of the parcels within the conduit. Parcel width decreases with increasing frequency; it is around 16 m, 8 m, and 4 m for 0.0625 Hz, 0.125 Hz, and 0.25 Hz, respectively. Therefore, the high crystallinity parcels in the lower frequency profiles make larger contributions to the seismic force. Similar reasoning explains why the low crystallinity parcels in lower frequency injections lead to greater reduction in the upward seismic force than for the higher frequency injections.

Radial and vertical seismograms, shown in Figure 16, are dominated by force contributions. Displacement seismograms display a similar trend to the seismic force with amplitude decreasing with increasing injection frequency. The nonlinear system response to the sinusoidal input is reflected in the displacement seismograms (becoming more apparent at higher frequencies) and it is even more pronounced in the velocity seismograms. Looking in particular at the vertical velocity seismograms, the waveforms exhibit periodic cycles beginning with a rapid upward increase to peak velocity, followed by a trailing fall off in amplitude. With increasing injection frequency, these features sharpen and the peak particle velocity increases. For the 0.25 Hz injection profile, velocity amplitudes reach $\sim$1 μm/s, which are comparable with observed eruption tremor amplitudes (Fee, Haney, et al., 2017). The peaks correspond to the rupture of high crystallinity parcels passing through fragmentation, when the fragmentation front rapidly descends as the low crystallinity parcel approaches. The tails of the velocity peaks are produced when high crystallinity parcels approach fragmentation, creating resistance to flow as viscosity increases before fragmenting. The seismic velocity PSD (Figure 17) confirms the periodic nature of the system output, with sharply defined peaks at the same frequency as the injection. Overtone peaks are due to the Dirac comb effect, when a signal is periodically repeated a finite number of times (Hotovec et al., 2013; Dmitrieva et al., 2013).

4.3 Stochastic profile

Now that we have an understanding of how heterogeneities at different frequencies affect the fragmentation dynamics and their expression in the seismic response, we move on to a stochastic injection profile. For the exponential autocorrelation model, we choose the standard deviation ε so that crystal volume fraction variations are of comparable amplitude as in the sinusoidal examples. We investigate how the correlation timescale t_{cor} affects the seismic signal by considering two simulations with $t_{\mathrm{cor}} = 1$ s and 10 s. Figures 18 and 19 show the PSD and time series, respectively, of the particular realization of the stochastic profile used in this study. In our simulations, the inlet velocity is approximately 1 m/s; therefore, these correlation timescales can be thought of as correlation length scales of 1 m and 10 m, respectively. The particular realizations of the random signal used in our simulations are shown in Figures 18 and 19. To reduce computational expense, we have chosen a cutoff frequency of 0.25 Hz in order to ensure that no numerical artifacts are introduced due to insufficient spatial resolution. The 10 s cor-

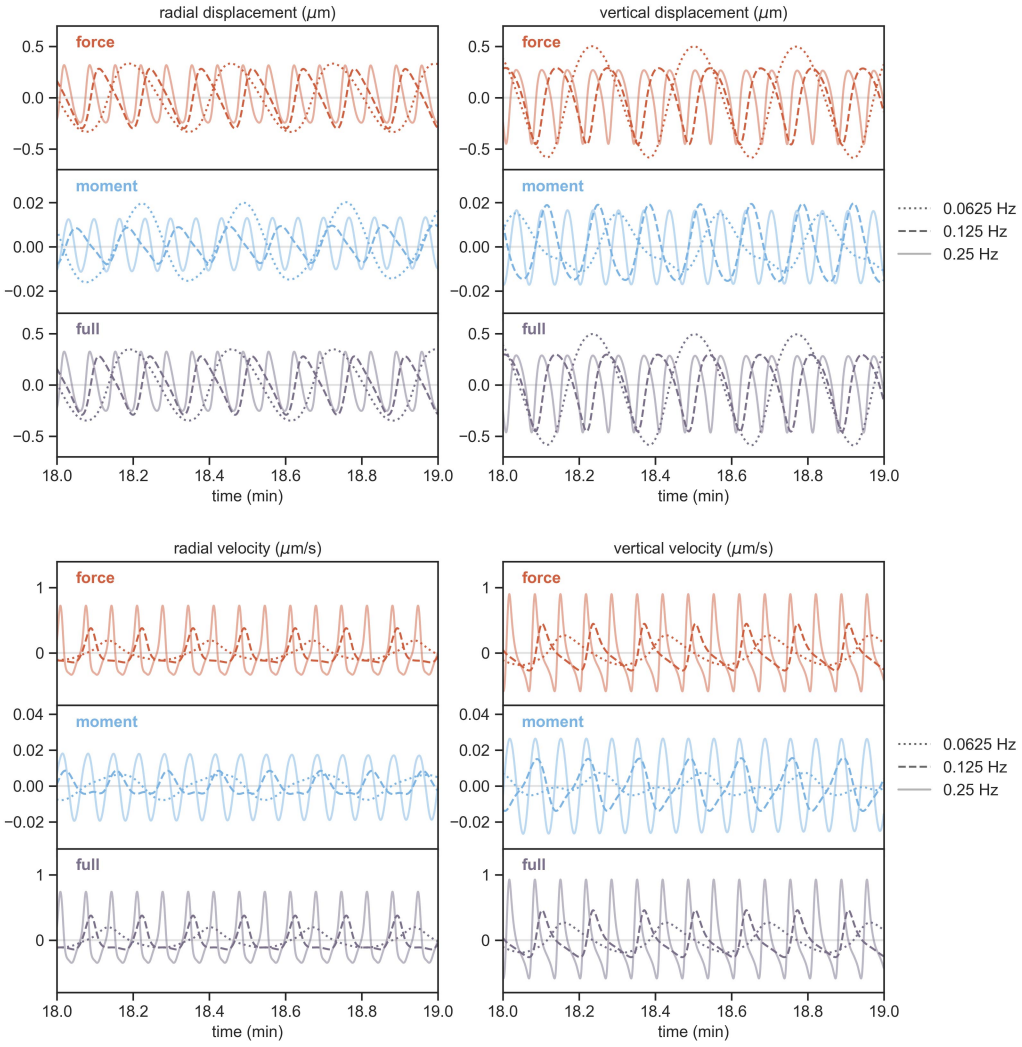

Figure 16. Synthetic displacement and velocity seismograms for different frequency sinusoidal injections at a receiver 10 km from vent. Static offsets in displacement seismograms have been removed (i.e., de-meaned).

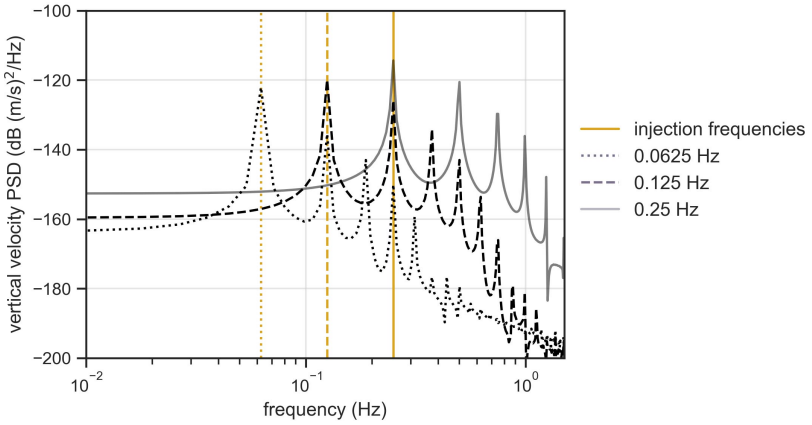

Figure 17. Power spectral densities of vertical velocity seismograms for different frequency sinusoidal injections. Yellow lines mark the injection frequencies.

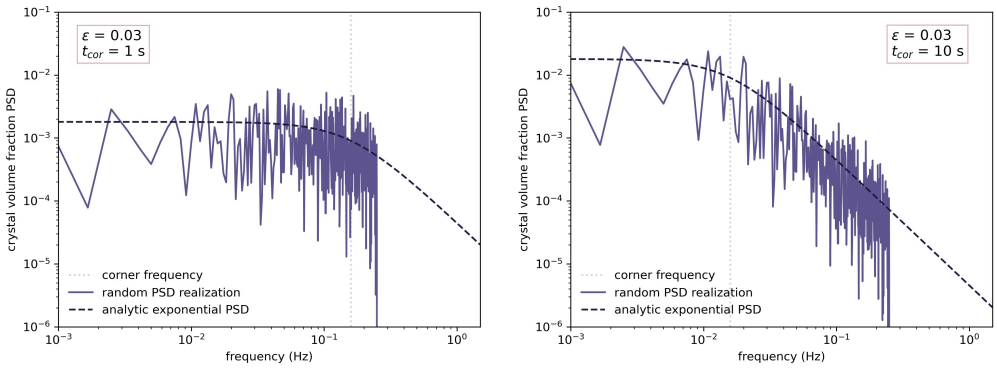

Figure 18. Power spectral densities of stochastic crystal volume fraction fluctuation profiles with different correlation timescales.

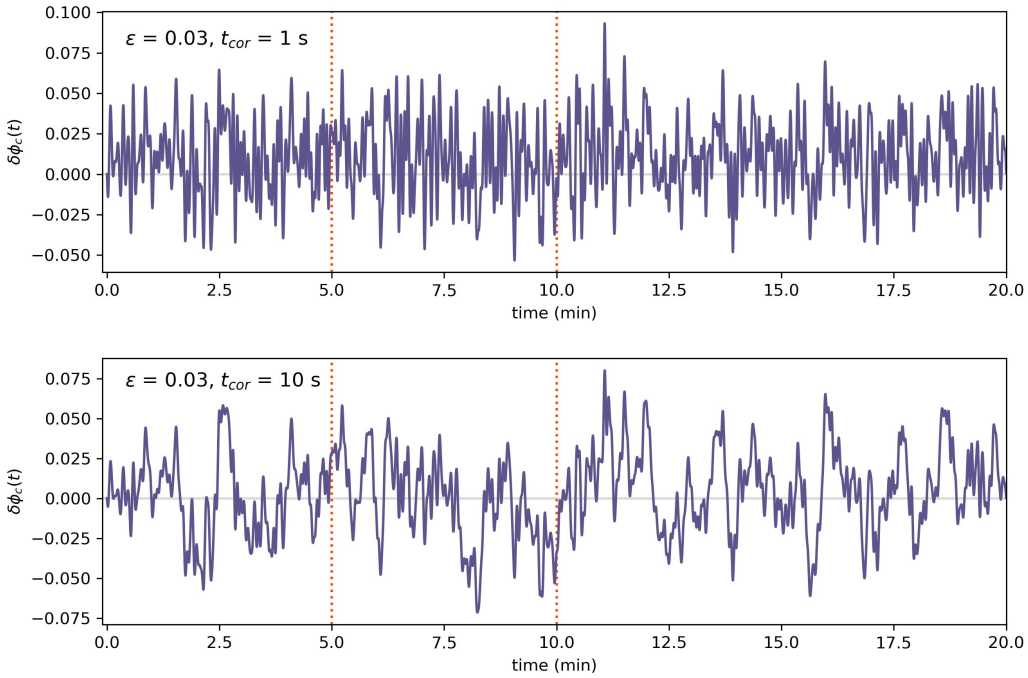

Figure 19. Time-domain realization of stochastic crystal volume fraction fluctuation profile with different correlation timescales. Red dotted lines mark the heterogeneities that are passing through fragmentation during the time windows shown in subsequent plots.

relation timescale yields greater power in the lower frequency range, with steeper fall-off in power at higher frequencies. The shorter correlation timescale of 1 s yields a relatively flat spectrum within the resolvable frequency band. The greater power at low frequencies for the 10 s correlation timescale is also apparent when comparing the time domain realizations of the injection profiles (Figure 19).

As in the sinusoid case, we restrict attention to a time window after an initial "spin-up" period during which heterogeneities ascend and fully fill the conduit. The fragmentation front moves up and down in a stochastic manner, reflecting the range of frequencies contained in the heterogeneous profile. The higher power in the lower frequencies in the $t_{\rm cor} = 10$ s simulation leads to longer length-scale variations in crystal content. This leads to longer period motion of the fragmentation front (Figures 22 and 23), which oscillates over a depth range of 25 m over the course of 5 minutes. In the $t_{\rm cor} = 1$ s simulation, the fragmentation motion is reflective of the flatter injection spectrum with higher frequency motion providing a comparable contribution as the longer periods (Figures 20 and 21). The fragmentation front moves over a depth range of 15 m over the course of 5 minutes. The range of peak wall shear stress at fragmentation is comparable between the two cases, but the rate of change is greater for the shorter correlation timescale (Figures 21 and 23). In both cases, there is a lot of unsteadiness exhibited in the mass eruption rate as the stochastic heterogeneities pass through fragmentation. There are longer period trends in mass eruption rate for the 10 s correlation timescale associated with the long period crystal content variations. Also, in the particular time window selected for analysis, there is enhanced mass eruption rate as a lower crystal content region passes through fragmentation (Figure 22).

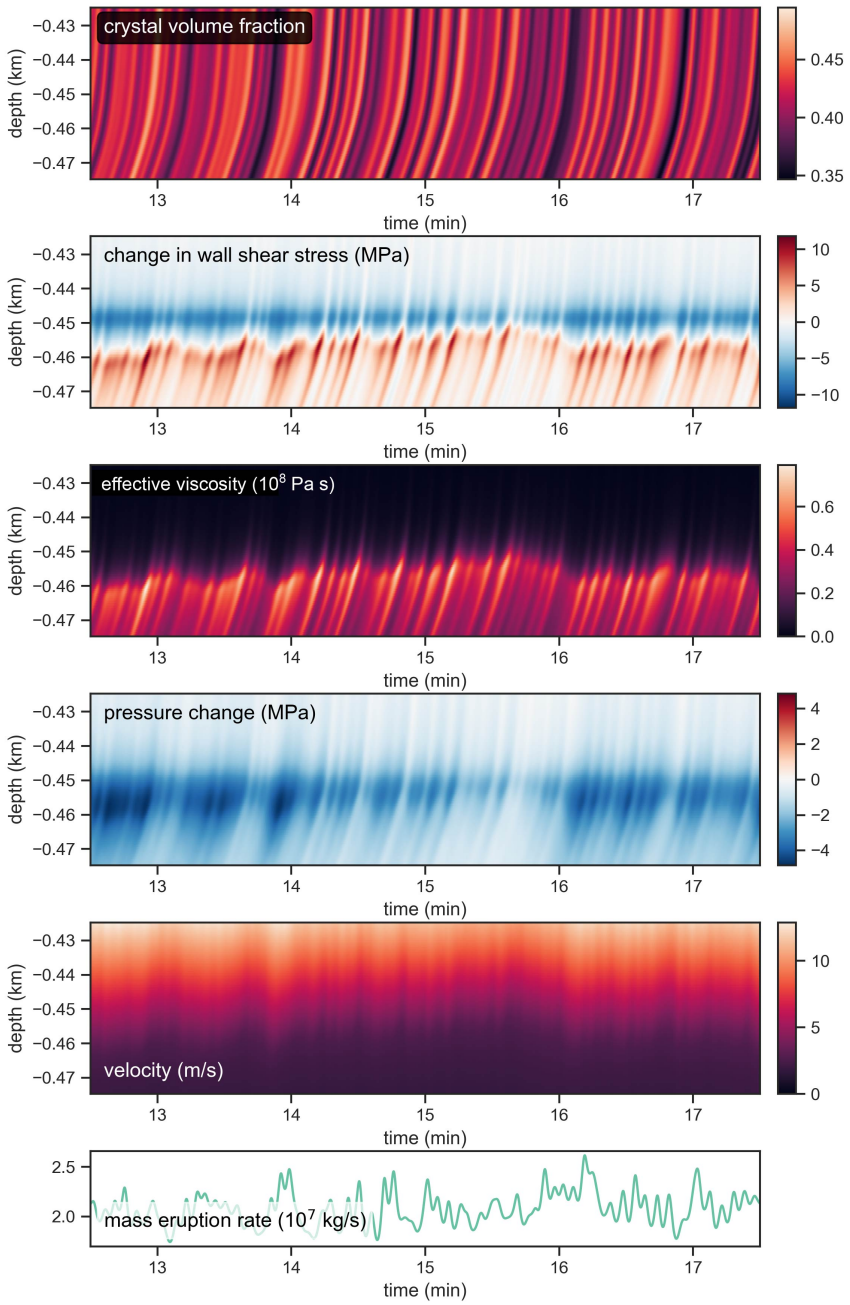

Figure 20. Stochastic injection simulation results for $t_{\mathrm{cor}} = 1$ s.

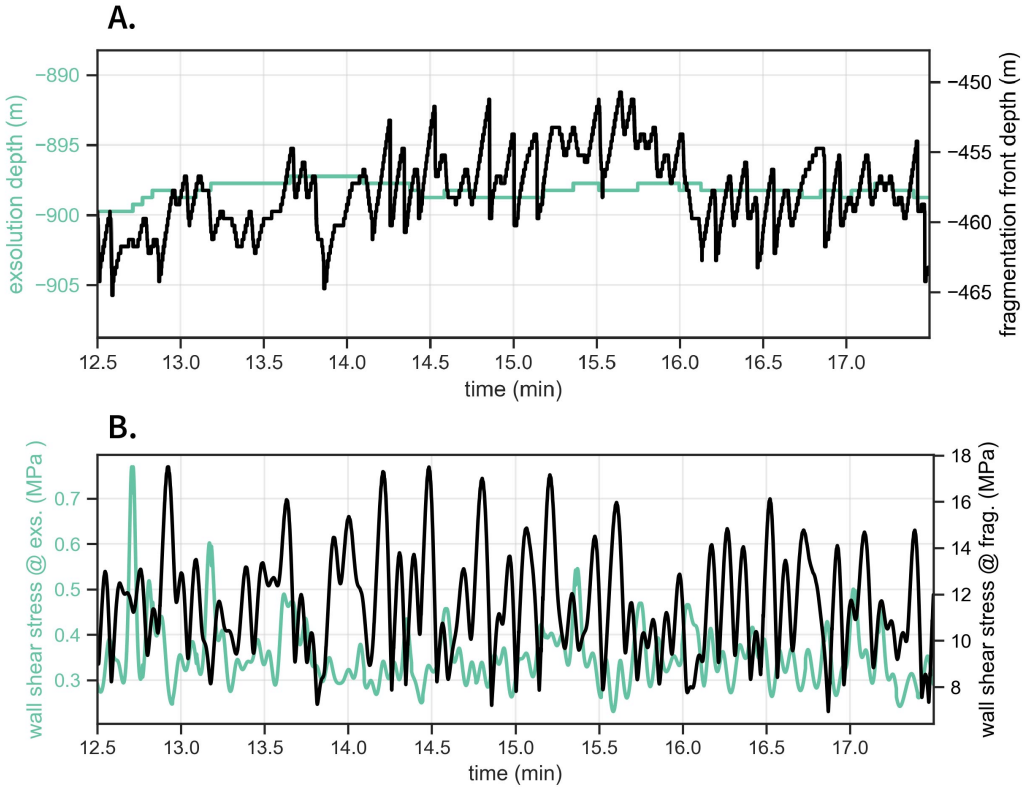

Figure 21. Fragmentation and exsolution depth evolution with time for stochastic injection simulation with $t_{\text{cor}} = 1$ s: **A.** Fragmentation and exsolution depths. **B.** Wall shear stress at fragmentation and exsolution depths.

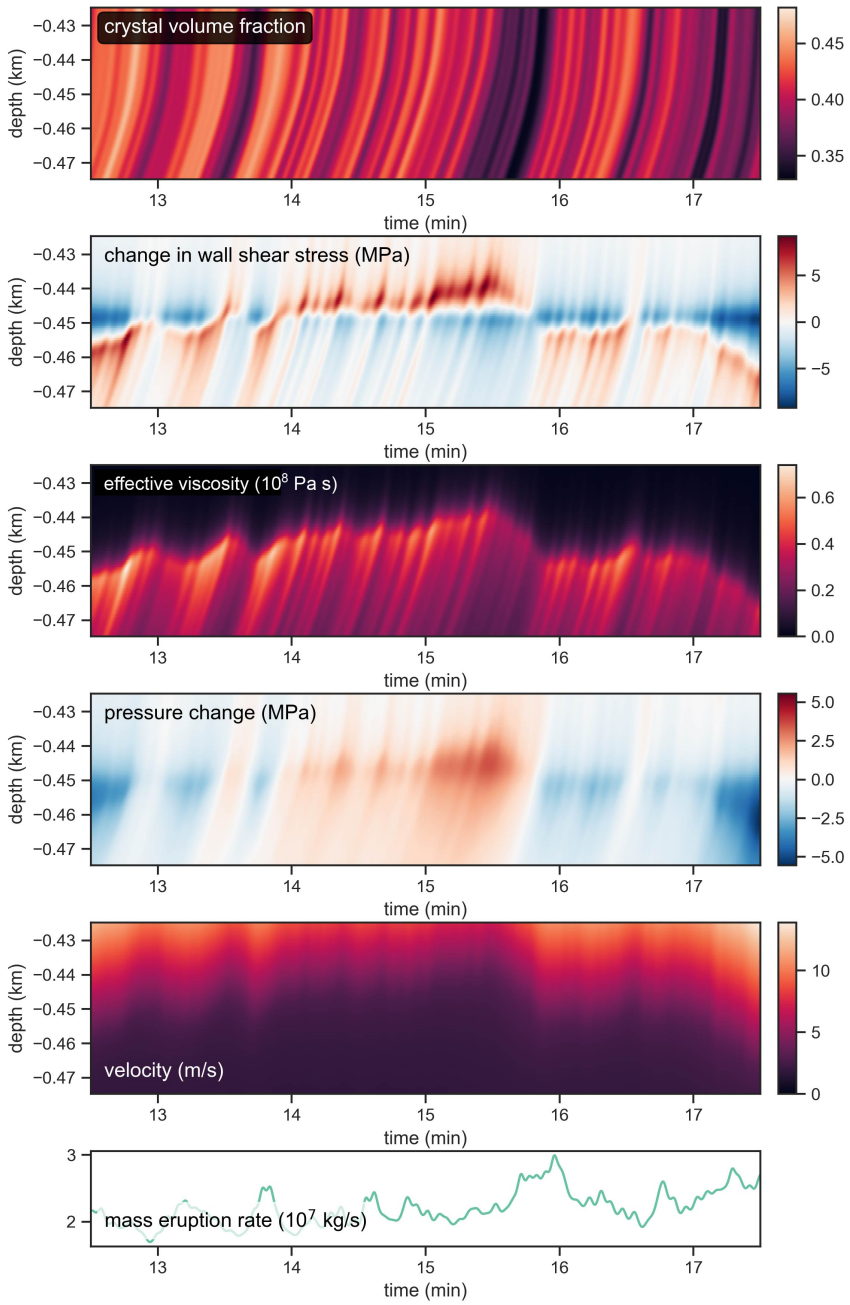

Figure 22. Stochastic injection simulation for $t_{\mathrm{cor}} = 10$ s.

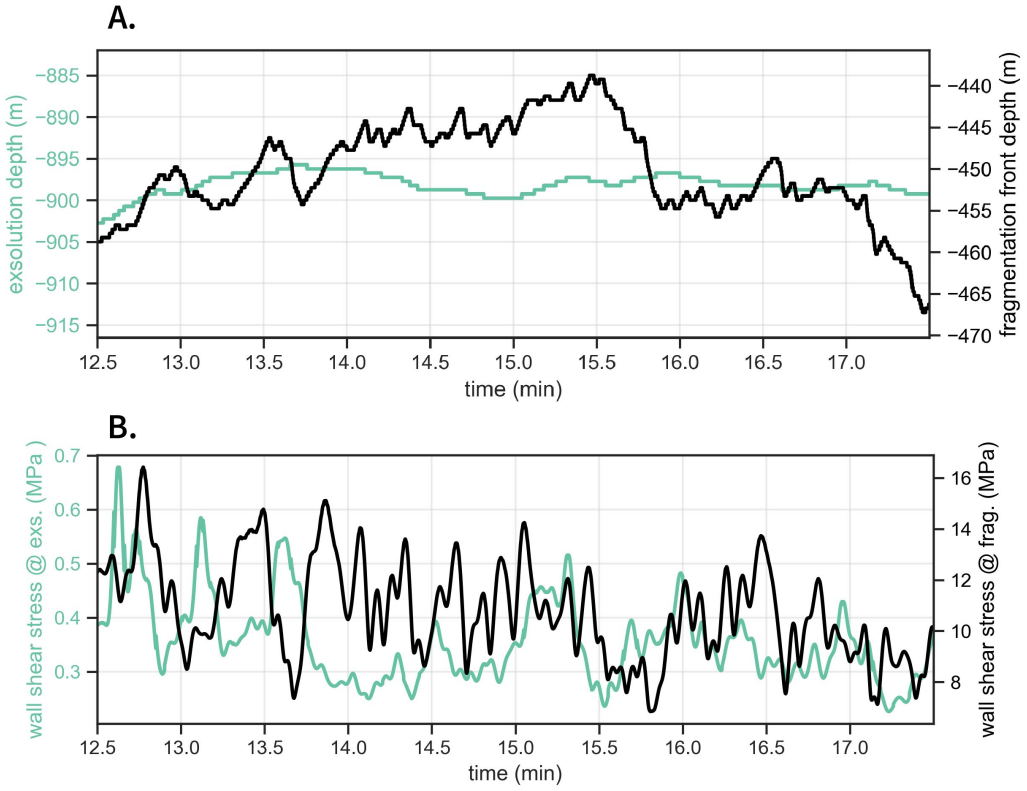

Figure 23. Fragmentation and exsolution depth evolution with time for stochastic injection simulation with $t_{\text{cor}} = 10$ s: **A.** Fragmentation and exsolution depths. **B.** Wall shear stress at fragmentation and exsolution depths.

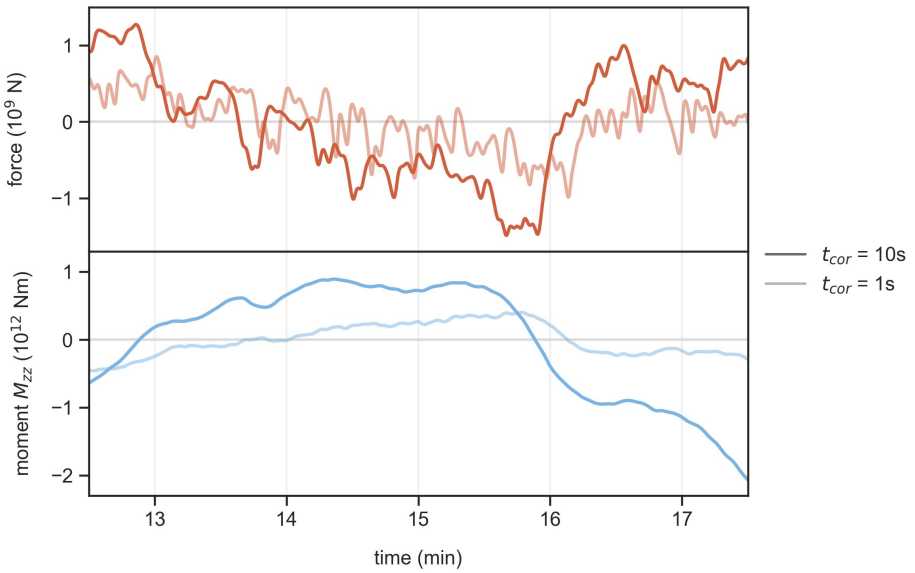

Figure 24. Seismic force and moment histories for stochastic injections with different correlation timescales. Force and moment histories have been de-meaned. The other nonzero moment tensor components, $M_{xx} = M_{yy}$, are proportional to M_{zz}.

The seismic force and moment histories (Figure 24) exhibit fluctuations over a larger range of values, as compared to the sinusoidal cases. The force ranges are comparable between the two correlation timescales, with $t_{\mathrm{cor}} = 10$ s exhibiting a slightly larger range. Even though the fragmentation depth moves over a greater range for $t_{\mathrm{cor}} = 10$ s, the peak wall shear stress (i.e., peak viscosities) are more frequently reached for $t_{\mathrm{cor}} = 1$ s. This is reflected in the force histories, where the shorter correlation timescale exhibits larger amplitude high frequency features. There is an overall reduction in upward force accompanied by an increase in moment in the first 3.5 minutes as the region of higher crystal content passes through fragmentation, reducing the total drag along the whole length of the conduit. While this is seen in both cases, it is particularly apparent for the longer correlation timescale case. This is similar to the Gaussian pulse simulations. We can draw an analogy to a wider pulse with small scale variations around that longer period feature. Immediately following the time window shown here, a region of higher crystal content follows (Figure 19). The precursor features associated with the approach to fragmentation of a high crystal content region are seen in the force and moment histories (Figure 24): The seismic force increases as the high crystal content region approaches fragmentation and viscosity increases, which is accompanied by depressurization of the conduit above the region.

The vertical component of the displacement seismograms is dominated by the force contribution, capturing the full spectrum of the progression of the heterogeneities through fragmentation (Figure 25). The radial displacement has comparable contributions from the force and moment. Radial displacements associated with the pressurization/depressurization of the conduit are dominated by low frequencies, leading to preservation of high frequency features from force changes along the conduit walls in the full waveform. The displacement amplitudes are comparable for the two correlation timescale simulations, with the shorter timescale simulation exhibiting more prominent high frequency features. Velocity seismograms highlight these high frequency features.

The vertical velocity power spectral densities (PSDs) (Figure 26) confirm the boosting of higher frequencies for the shorter correlation timescale simulation. The crystal injection PSDs (Figure 18) have a flat spectrum at frequencies below the corner frequency, above which the spectrum follows a power-law decrease. However, the seismic spectra are either flat ($t_{\mathrm{cor}} = 10$ s) or slightly increasing ($t_{\mathrm{cor}} = 1$ s) beyond the injection corner frequency, until they roll over at the injection cut-off frequency (0.25 Hz). Power at low frequencies is comparable between the two correlation timescales but slightly higher for $t_{\mathrm{cor}} = 10$ s. For higher frequencies (> 0.1 Hz), $t_{\mathrm{cor}} = 1$ s has greater power that peaks around the injection corner frequency. The shorter correlation timescale yields a somewhat broader spectrum that is pushed further out beyond the injection cut-off frequency.

5 Discussion

5.1 Model validation and relation to other observables

Because our modeling framework couples conduit flow dynamics to seismic wave generation, we are able to draw connections between seismic signals and other observables, providing observationally testable predictions. In addition to predictions of distinct seismic signatures in the VLP and ULP bands, our work makes predictions of coincident mass eruption rate fluctuations associated with fluctuations in fragmentation. Estimates of mass eruption rate can be made using visual and thermal monitoring of eruption plumes (e.g., Vulpiani et al., 2016; Freret-Lorgeril et al., 2021) or through gas emissions measurements (Hobbs et al., 1991; Mori & Burton, 2009; Fee, Izbekov, et al., 2017; Reath et al., 2021; Raponi et al., 2021). Correlations between VLP signals and variations of volcanic gas emissions have been observed at Mt. Asama, Japan (Kazahaya et al., 2011). The observed VLP velocity waveforms – similar in duration and shape to those

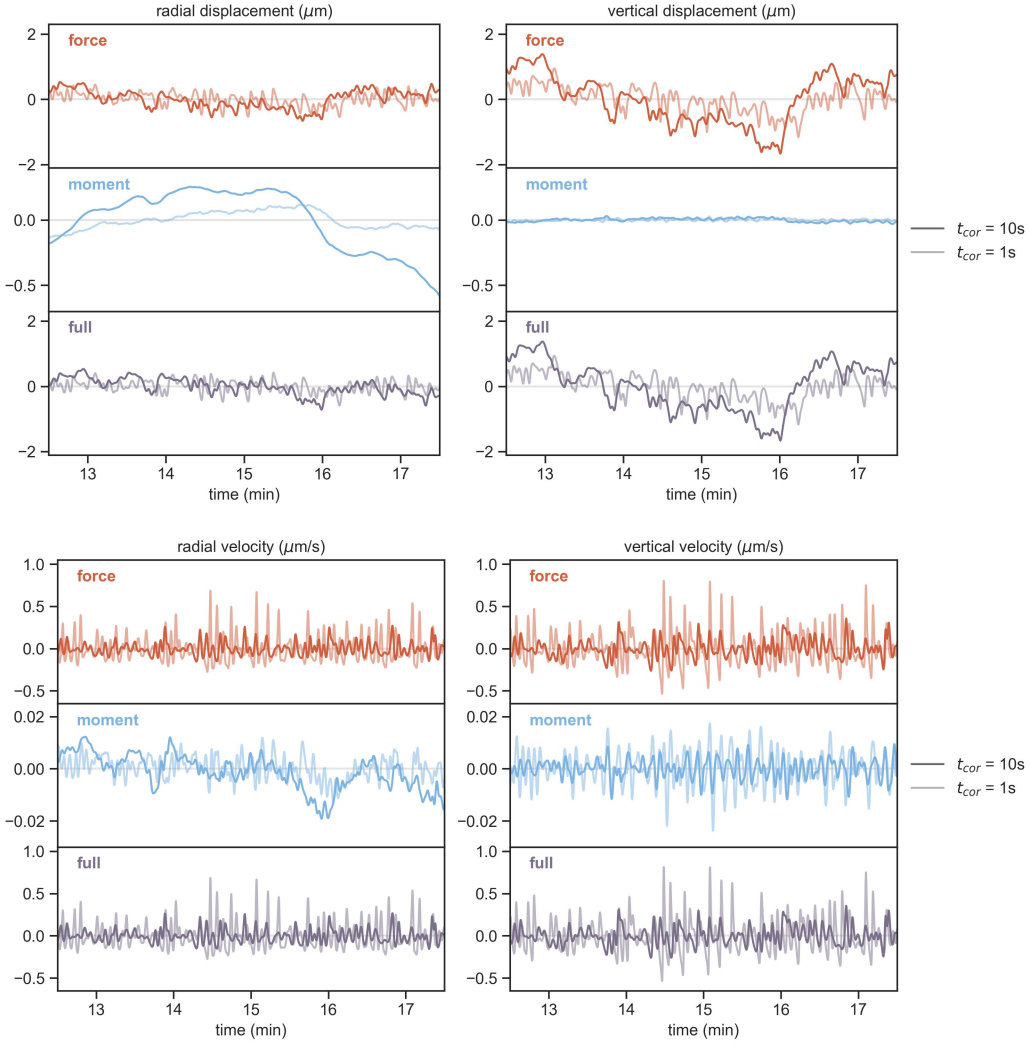

Figure 25. Synthetic displacement and velocity seismograms for stochastic injections with different correlation timescales at a receiver 10 km from vent. Static offsets in displacement seismograms have been removed (i.e., de-meaned).

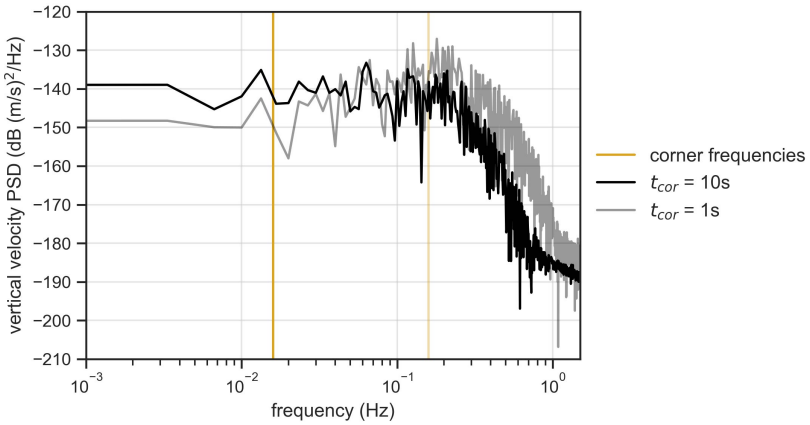

Figure 26. Power spectral densities of vertical velocity seismograms for stochastic injections with different correlation timescales. Yellow lines mark the corner frequencies for the injection spectra.

predicted in this work – were followed by enhanced SO_2 flux through the vent, which might be explained by unsteady fragmentation in response to the development of overpressure from magma degassing. The scale of variations in mass eruption rate predicted in this work ($\sim 10^7$ kg/s) would yield significant features in these additional measurements. Therefore, observations of VLP/ULP seismic signatures cross-checked with additional monitoring data for the eruption plume can be used to provide evidence for fluctuating fragmentation as a source of eruption unsteadiness. Extending our modeling above the vent, or coupling with a plume and atmospheric response model (Liu et al., 1982; Kanamori et al., 1994; Ripepe et al., 2010; Nakashima et al., 2016), would yield further quantitative predictions for validation. Our modeling outputs include time-series for relevant fluid dynamic properties at the conduit vent (e.g., mass eruption rate, pressure) that define source processes through direct connection to modeled eruptive processes. This allows for predictions of any instabilities in the eruptive jet that might be triggered or caused by fluctuating fragmentation. In addition, it is possible that variations in mass eruption rate will also generate infrasonic signatures, which can then be used to further constrain characteristics of fluctuating fragmentation.

5.2 Coherent fluctuations in fragmentation

Our work predicts that coherent fluctuations in the fragmentation depth, as can be caused by coherent heterogeneities of magma properties such as the crystal content, are expressed seismically in the VLP and ULP frequency bands. In particular, fragmentation of a parcel of high crystal content magma produces a distinct VLP signature consisting of a downward pulse in vertical velocity seismograms. This is caused by a drop in the upward seismic force when the high viscosity parcel fragments. The duration of the seismic signal correlates with the width of the parcel, reflecting the time it takes for the parcel to fully pass through fragmentation. The particle velocity amplitudes are controlled by a combination of viscosity variation and parcel width (and seismic wave propagation parameters like source-receiver distance). Our simulations showed that parcels of the same relative viscosity but different widths will generate different peak amplitudes, with the smaller width yielding higher amplitude. However, it does not appear to be straightforward to disentangle these two contributions to seismic amplitude. Reductions in mass eruption rate associated with fragmentation of high crystal content parcels provide another means to help constrain viscosity variations. The same reduction in mass eruption

rate is predicted for different parcel widths having the same relative viscosity. Similarly to the seismic signatures, the duration of the mass eruption rate reduction is correlated with parcel width. Therefore, coincident VLP/ULP signatures and mass eruption rate variations provide potential diagnostics to characterize coherent magma heterogeneities.

As discussed in the previous section, validation of this source mechanism will involve looking for coincident signatures in seismic, visual/thermal, infrasound, and gas emissions data. Advection and fragmentation of heterogeneous magma could occur at any point during an eruption. Thus, observations of VLP signatures during a sustained eruption (in contrast to VLP signatures produced by the eruption onset) – along with observed changes in mass eruption rate – could potentially be generated by this source mechanism. Further potential validation could come from petrological study of eruption deposits. This would be done by checking the composition (Pankhurst et al., 2014) for variations in crystal content or other differences in erupted products from the specific time interval marked by the VLP and mass eruption rate signals. This also points to the potential utility of combining petrological study with these geophysical signals. The amplitude and duration of geophysical signals could help to constrain estimates of volumes of different erupted products. The timing of coincident signatures within the eruption sequence – along with visual observations of erupted materials – can be used when reconstructing the compositional evolution of the volcanic deposits. The reconstructed erupted materials sequence could then be used to make inferences about the sourcing magma body, such as the magma storage conditions (Bachmann & Huber, 2019; Popa et al., 2021). The spectral content of the geophysical signatures could potentially be used to infer length scales of heterogeneities present in the sourcing magma body, which may give valuable information on magma mixing processes (Perugini & Poli, 2012; Morgavi et al., 2022).

5.3 Eruption tremor

Eruption tremor is a seismic signal ubiquitously observed during explosive eruptions (McNutt & Nishimura, 2008; Konstantinou & Schlindwein, 2003). In addition to its coincidence with explosive eruptive activity, it is characterized by its stochastic nature within the 0.5-10 Hz frequency band. (We discuss another form of tremor, harmonic tremor, in the next section.) There have been very few theoretical studies on the source of eruption tremor (McNutt & Nishimura, 2008; Prejean & Brodsky, 2011; Gestrich et al., 2020). One of the only physical models proposed attempts to recreate seismic PSDs through defining force spectra from particle impacts and dynamic pressure changes due to turbulence along the conduit walls (Gestrich et al., 2020). Focus was restricted to the upper conduit above the fragmentation depth, where flow is turbulent. The authors found that the traction fluctuations required to explain observed tremor amplitudes required extreme parameter values, such as impacting particle sizes of $\sim$1 m. While this hypothesized mechanism for eruption tremor is plausible, we feel that it is important to explore alternative hypotheses. Our work shifts focus to the fragmentation depth and just below it, where tractions are orders of magnitude higher and motion of the fragmentation front can produce requisite amplitudes of force fluctuations. We can no longer appeal to turbulence to explain stochasticity for this mechanism; therefore, stochastic motion of the fragmentation front is required.

Our modeling shows that stochastic fluctuations in fragmentation do in fact lead to stochastic seismic signals. For $\sim$7.5 % fluctuations in crystal content, seismic particle velocities at a few to 10 km distance are on the order of 0.1 μm/s, which is about an order of magnitude less than observed tremor amplitudes. However, our simulations were limited to frequencies below 0.25 Hz due to numerical resolution requirements and computational cost. Our sinusoidal injection study highlighted that shifting power to higher frequencies could yield seismic amplitudes that are relevant to observed tremor ($\sim$1 μm/s) (Fee, Haney, et al., 2017; Konstantinou & Schlindwein, 2003). Given the limitations of our simulations, it is premature to falsify or validate our proposed mechanism for erup-

tion tremor. That said, our results do serve as proof-of-concept that fluctuating fragmentation could be a potential source of eruption tremor, especially if higher frequency fluctuations are included.

Extending to higher frequencies with observationally relevant power could be done in a couple of ways. Increasing the cutoff frequency of the crystal content fluctuations will broaden the seismic spectrum, which will likely increase seismic amplitudes with the introduction of higher frequency variations. In addition to that, one possibility is to consider smaller correlation timescales for heterogeneous injection. The associated corner frequency for a correlation timescale on the order of 10^{-2} s would reach the upper end of the characteristic tremor frequency range. For an inlet velocity of 1 m/s, this would correspond to a correlation length-scale on the order of centimeters for heterogeneity within the sourcing magma body. Of course, for heterogeneity length scales smaller than the conduit radius, the quasi-1D modeling assumption breaks down. The fragmentation surface will have more complex geometry than can be captured in our quasi-1D conduit flow model, and the distribution of wall shear stress will no longer be axisymmetric. These additional complexities become relevant at frequencies ≥ 1 Hz. Modeling these fluctuations will require moving to a 3D framework that is able to capture the cross-sectional variations that may be present during the fragmentation process.

5.4 Harmonic tremor

Harmonic tremor is another seismic signal occasionally observed at some volcanoes, characterized by sustained oscillations with distinct spectral peaks (Konstantinou & Schlindwein, 2003; Chouet & Matoza, 2013). Our study of sinusoidal injection profiles hints at the possibility that periodic movement of the fragmentation front would yield harmonic tremor. While it is unlikely that magma heterogeneity would exhibit this regularity, there could be other self-excited instabilities or forced oscillations that emerge naturally from the system. For instance, oscillations or "wagging" of the rising magma column in response to spring-like motion of a compressible bubble-rich annulus along the conduit walls has been proposed as a possible harmonic tremor mechanism (Bercovici et al., 2013). Naturally emerging oscillatory dynamics have been observed in studies of detonation shock-wave propagation (Kasimov & Gonchar, 2021), a process that is somewhat analogous to fragmentation. Alternative fragmentation criteria to the critical volume fraction criterion used in this work (Melnik & Sparks, 2002; Jones et al., 2022; Alidibirov & Dingwell, 2000; Papale, 1999; Fowler et al., 2010; Scheu & Dingwell, 2022; Lavallée & Kendrick, 2021; McGuinness et al., 2012; Koyaguchi et al., 2008; Gonnermann, 2015; Gonnermann & Manga, 2003, 2007) may lead to oscillatory behavior, though almost all of these criteria have only been investigated using steady-state models. One exception is the unsteady conduit flow modeling of Melnik and Sparks (2002) that was designed for vulcanian explosion events. They compared the critical volume fraction criterion to two alternatives, a critical bubble overpressure criterion and a critical elongation strain rate criterion. They found that while the volume fraction criterion produced smoothly varying fragmentation, the other two criteria produced pulsatory solutions. Further study of fragmentation and associated seismic signals could be utilized to constrain characteristics of the particular mechanism, which is still an open science question.

6 Conclusion

In this study, we explored the seismic signatures of a fluctuating fragmentation in explosive volcanic eruptions. Fragmentation depth fluctuations are associated with changes in pressure and wall shear stresses, which are proportional to the seismic moment and force, respectively. Seismograms at a few to ∼10 km distances are in most cases dominated by the seismic force, which has contributions arising from changes in fragmentation depth and from variations in wall shear stress. Through simulations of advection

and fragmentation of heterogeneous magma using unsteady conduit flow models, we demonstrated that heterogeneous magma injections could be a source of fluctuating fragmentation. Our work predicts that distinct seismic VLP signatures and coincident variations in mass eruption rate accompany coherent fluctuations in the fragmentation depth, providing useful observational diagnostics for validation. Our work also demonstrated that stochastic movement of fragmentation leads to stochastic seismic signals. This provides a plausible mechanism for eruption tremor. However, numerical resolution constraints prevented us from exploring frequencies greater than 0.25 Hz, which must be done to properly test this hypothesis. Overall, we have demonstrated how unsteady conduit flow modeling can be integrated into volcano seismology studies. This dynamic source modeling approach complements kinematic source inversions, providing a more direct relation between eruptive processes of interest and seismograms.

Appendix A Governing equations for unsteady multi-phase conduit flow model with variable viscosity

This appendix lays out the governing equations for the conduit flow model used in this work. We model adiabatic multi-phase flow through a cylindrical conduit using a quasi one-dimensional unsteady conduit flow model solved using Quail, a discontinuous Galerkin solver for hyperbolic partial differential equations (Ching et al., 2022). The mixture is composed of multiple phases: exsolved water, liquid melt, dissolved water, and crystals. We use "magma" to refer to the combination of liquid melt, dissolved water, and crystals. We assume that the exsolved water and magma share the same temperature and pressure at a given point.

The top pressure boundary condition is set to atmospheric pressure (10^5 Pa), when flow through the vent is subsonic. When exit velocity is sonic, the flow is choked. The bottom boundary conditions consist of an imposed constant pressure (i.e., chamber pressure) as well as specification of the mass fractions of each phase, which can be varied in time. See Section 3.2 for specifics on how magma composition is specified at the bottom boundary. Note that governing equations are formulated in terms of partial densities of each phase: the mass of the phase relative to the total volume.

A1 Mass balance

The governing equations include a mass balance for each of the phases in the mixture. We assume the same phasic density for liquid melt, dissolved water, and crystals. The magma mass balance captures the loss of mass through exsolution of water:

$$\frac{\partial \overline{\rho}_{\text{mag}}}{\partial t} + \frac{\partial (\overline{\rho}_{\text{mag}} v)}{\partial z} = -\overline{\rho}_{\text{melt}} \left(\frac{\chi_d - \chi_{\text{eq}}(p)}{t_{\text{ex}}} \right), \tag{A1}$$

where $\overline{\rho}_{\text{mag}}$ is the partial density of magma, χ_d is the mass concentration of dissolved water (mass of dissolved water / mass of melt), $\overline{\rho}_{\text{melt}}$ is the partial density of liquid melt, $\chi_{\text{eq}}(p)$ is the equilibrium mass concentration of dissolved water at pressure p, v is the mixture particle velocity, and t_{ex} is the timescale of exsolution. The equilibrium mass concentration of dissolved water is described by Henry's law of solubility:

$$\chi_{\text{eq}}(p) = \min(\chi_0, S_m p^{1/2}) \tag{A2}$$

where χ_0 is the total water mass concentration and S_m is the solubility constant. Magma phasic density ρ_{mag} (i.e., mass of magma relative to magma volume) is determined by a linearized equation of state:

$$p = p_0 + \frac{K}{\rho_{\text{mag},0}} (\rho_{\text{mag}} - \rho_{\text{mag},0}), \tag{A3}$$

where $\rho_{\text{mag},0}$, K, and p_0 are the reference magma density, bulk modulus, and reference pressure, respectively. Water is exchanged between the magma and the exsolved water

phases, which is also captured in the mass balance for exsolved water:

$$\frac{\partial \overline{\rho}_{\mathrm{ex}}}{\partial t} + \frac{\partial (\overline{\rho}_{\mathrm{ex}} v)}{\partial z} = \overline{\rho}_{\mathrm{melt}} \left(\frac{\chi_d - \chi_{\mathrm{eq}}(p)}{t_{\mathrm{ex}}} \right), \tag{A4}$$

where $\overline{\rho}_{\mathrm{ex}}$ is the partial density of exsolved water. The total water content (dissolved plus exsolved) is governed by a source-free mass balance:

$$\frac{\partial (\overline{\rho}_w)}{\partial t} + \frac{\partial (\overline{\rho}_w v)}{\partial z} = 0, \tag{A5}$$

where $\overline{\rho}_{\mathrm{w}}$ is the partial density of total water. This assumes there is no gas escape or introduction of other sources of water throughout the eruption. Exsolved water obeys an ideal gas equation of state, despite being in a supercritical state in the lower portion of the conduit:

$$p = \rho_{\mathrm{ex}} R_G T, \tag{A6}$$

where ρ_{ex} is the phasic density of exsolved water, R_G is the specific gas constant, and T is temperature. We initialize the conduit magma with a specified crystal content, which is advected through the conduit following a source-free mass balance:

$$\frac{\partial \overline{\rho}_c}{\partial t} + \frac{\partial (\overline{\rho}_c v)}{\partial z} = 0, \tag{A7}$$

where $\overline{\rho}_c$ is the partial density of crystals. We do not simulate crystallization kinetics during the eruption.

A2 Momentum and energy balance

The governing equations also include the momentum balance for the mixture, which is sufficient due to the assumption that all phases are co-moving and share a common pressure, temperature, and velocity. The momentum balance is

$$\rho \left(\frac{\partial v}{\partial t} + v \frac{\partial v}{\partial z} \right) = -\frac{\partial p}{\partial z} - \rho g - \frac{2\tau}{R}, \tag{A8}$$

where τ is wall shear stress, ρ is mixture density, v is mixture particle velocity, R is radius of conduit, and p is pressure. Fragmentation of the mixture is captured in the definition of wall shear stress, which turns off when the mixture has met the critical gas volume fraction threshold.

Similarly, we use a single energy balance equation for the mixture:

$$\frac{\partial e}{\partial t} + \frac{\partial ((e+p)v)}{\partial z} = -\rho g v - \frac{2\tau v}{R}, \tag{A9}$$

where e is the total energy (internal plus kinetic) per unit volume for the mixture. Internal energy per unit volume for the mixture is

$$e_{\mathrm{internal}} = \overline{\rho}_{\mathrm{ex}} C_{\mathrm{v,ex}} T + \overline{\rho}_{\mathrm{mag}} C_{\mathrm{v,mag}} T, \tag{A10}$$

where $C_{\mathrm{v,ex}}$ and $C_{\mathrm{v,mag}}$ are heat capacities for exsolved water and magma, respectively.

Fragmentation poses some numerical challenges, as it is a region with very sharp spatial gradients as the flow transitions from laminar to turbulent and the wall shear stress drops from its highest value to zero. We observed in the conduit flow model used in Coppess et al. (2022), that when the spatial resolution insufficiently resolves the fragmentation region, we see numerical features dominating the signal. Coppess et al. (2022) resolved this with a smoothing function for the drag turn-off in the form of a logistic function. However, this method did not lead to full turning off of the friction above fragmentation due to smearing never returning to zero. To remedy this and to introduce a tuning parameter that is more physically intuitive, we introduce a new smoothing method

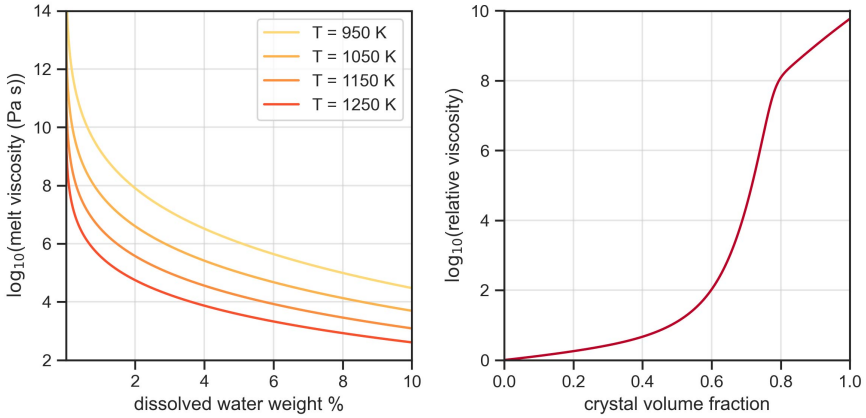

Figure A1. Viscosity dependence on magma composition. On left, melt viscosity (with no crystals) as a function of dissolved water content according to (A15) for different melt temperatures. On the right, relative viscosity as function of crystal volume fraction, according to (A16).

by introducing a new tracked quantity to record the progression of fragmentation, which we call the fragmented phase. This represents the partial density of fragmented magma and is passively advected through the conduit, only entering into the main governing equations through the wall shear stress. The evolution of this phase captures the dependence on gas volume fraction:

$$\frac{\partial \overline{\rho}_f}{\partial t} + \frac{\partial (\overline{\rho}_f v)}{\partial z} = h(\overline{\phi} - \overline{\phi}_0) \left(\frac{\overline{\rho}_{\text{mag}} - \overline{\rho}_f}{t_f} \right) \tag{A11}$$

where $\overline{\rho}_f$ is the partial density of the fragmented phase, t_f is the fragmentation timescale, $\overline{\phi}$ is gas volume fraction (i.e. volume of exsolved water relative to total volume), $\overline{\phi}_0$ is the critical gas volume fraction, and $h(x)$ is a smoothing function of the following form:

$$h(x) = \frac{g(x/\zeta + 1)}{g(x/\zeta + 1) + g(-x/\zeta)}, \; g(x) = \begin{cases} e^{-1/x} & x > 0 \\ 0 & x \leq 0 \end{cases} \tag{A12}$$

This is basically a smoothed Heaviside function, where $h(x) = 0$ for $x < -\zeta$, $h(x) = 1$ for $x > 0$, and $h(x)$ is given by (A12) for $-\zeta < x < 0$. Therefore, when $\overline{\phi} > \overline{\phi}_0$, $h(\overline{\phi} - \overline{\phi}_0) = 1$. When the gas volume fraction is well below the threshold ($\overline{\phi} < \overline{\phi}_0 - \zeta$), the fragmented phase remains zero and does not evolve in time. Once the exsolved gas volume fraction is within range of the critical gas volume fraction that marks the fragmentation transition ($\overline{\phi} \geq \overline{\phi}_0 - \zeta$), the fragmented phase source term is gradually turned on and the fragmented phase partial density is pulled towards the magma partial density over some fragmentation timescale; this simulates a fragmentation process with some finite timescale. We then use the ratio of the fragmented phase to the magma phase to turn off the wall shear stress τ, marking a gradual transition between the two flow regimes:

$$\tau = \frac{4\eta v}{R} \left(1 - \frac{\overline{\rho}_f}{\overline{\rho}_m} \right). \tag{A13}$$

The wall shear stress term also depends on the magma composition through viscosity. A common definition of viscosity used in conduit models takes the following form (Costa, 2005):

$$\eta = \eta_l(\chi_d, T)\eta_c(\phi_c), \tag{A14}$$

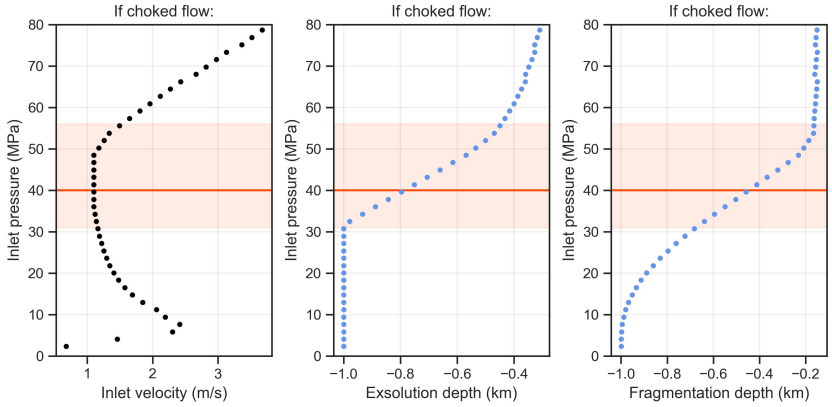

Figure B1. Steady state solution space for choked flow at the vent for a 1 km conduit. Time to fragmentation depth is approximated by (bottom of conduit - fragmentation depth) / inlet velocity. Shaded region indicates where both exsolution and fragmentation depths are contained within the simulated domain. Red line marks the particular solution used in this work, which is shown in more detail in Figure 2.

where η_l is the viscosity of melt without crystals as a function of dissolved water mass concentration χ_d and temperature T, and η_c is the relative viscosity as a function of crystal volume fraction ϕ_c (i.e., volume of crystals relative to magma volume). Hess and Dingwell (1996) performed an experimental study on viscosity of silicate melts, developing an empirical function capturing the relation between melt viscosity and dissolved water content without the presence of crystals:

$$\log \eta_l(\chi_d, T) = (-3.545 + 0.8333 \ln W_d) + \frac{(9601 - 2368 \ln W_d)}{T - (195.7 + 32.25 \ln W_d)}, \; W_d = 100\chi_d. \quad \text{(A15)}$$

Similar experimental studies have been performed to investigate the effect of crystals on the mixture viscosity. Similarly, Costa (2005) designed a functional form for the relative viscosity from crystal content, which was then fit to experimental data:

$$\eta_c(\phi_c) = \frac{1 + \left(\frac{\phi_c}{\phi_*}\right)^{\delta}}{\left\{1 - \alpha \, \mathrm{erf}\left(\frac{\sqrt{\pi}}{2\alpha} \frac{\phi_c}{\phi_*} \left[1 + \left(\frac{\phi_c}{\phi_*}\right)^{\gamma}\right]\right)\right\}^{B/\phi_*}} \quad \text{(A16)}$$

where B is the Einstein coefficient (2.5), ϕ_* is the critical transition fraction (0.673), and α, δ, γ are adjustable parameters (0.999916, 16.9386, 3.98937, respectively).

Appendix B Arriving at a steady-state solution for initialization

This section provides an overview of our approach to select a steady-state solution to initialize simulations. It is common for flow to be choked (i.e., fluid is traveling at sound speed) at the vent in explosive eruptions, which has the benefit of simplifying modeling by avoiding the need to model the eruptive jet and plume. We solve the steady-state version of the governing equations numerically, with choked flow at the top (or subsonic flow at atmospheric pressure at the top, if the choked flow pressure would be below atmospheric). Figure B1 shows characteristics of steady state solutions that satisfy the choked flow requirement. As part of the bottom boundary conditions, we can specify either the inlet velocity or pressure. Figure B1 shows that the steady state solution space is multi-valued in inlet velocity. Therefore, we define the steady state solution using an inlet pressure

condition. This also is a more natural formulation of the problem, as assuming constant (or slowly varying) pressure is a more realistic approximation for a conduit coupled to a magma chamber rather than constant velocity. Parameter values were chosen to balance being within observed ranges and reducing computation time. The bottom pressure boundary condition was chosen to be within 10 MPa of lithostatic pressure. The chosen solution is indicated by the red line in Fig. B1. To simplify defining the composition of magma injected through the bottom boundary, we require that the exsolution depth is fully contained within the simulation domain, in addition to the fragmentation depth (shaded region in Fig. B1). Crystal volume fraction $\overline{\phi}_c$ is constant with depth.

Acknowledgments

This work was funded by the National Science Foundation (DGE-1656518 to Katherine Coppess, EAR-1930979 and EAR-2231849 to Eric M. Dunham). Computer simulations were performed on Stanford's Sherlock cluster and we gratefully acknowledge the support of staff at the Stanford Research Computing and funding from the Doerr School of Sustainability for these computational resources.

Data Availability Statement

The conduit flow code, synthetic seismogram calculation code, and simulation data for this work are hosted at the following (respectively): https://github.com/fredriclam/quail_volcano, https://github.com/kcoppess/synthetic-seismograms, and Zenodo (doi: 10.5281/zenodo.10681597).

References

Alidibirov, M., & Dingwell, D. (2000). Three fragmentation mechanisms for highly viscous magma under rapid decompression. *Journal of Volcanology and Geothermal Research*, *100*(1-4), 413–421. doi: 10.1016/S0377-0273(00)00149-9

Bachmann, O., & Huber, C. (2019). The inner workings of crustal distillation columns; the physical mechanisms and rates controlling phase separation in silicic magma reservoirs. *Journal of Petrology*, *60*(1), 3–18. doi: 10.1093/petrology/egy103

Bercovici, D., Jellinek, A. M., Michaut, C., Roman, D. C., & Morse, R. (2013). Volcanic tremors and magma wagging: gas flux interactions and forcing mechanism. *Geophysical Journal International*, *195*(2), 1001–1022. doi: 10.1093/gji/ggt277

Caplan-Auerbach, J., Bellesiles, A., & Fernandes, J. K. (2010). Estimates of eruption velocity and plume height from infrasonic recordings of the 2006 eruption of Augustine Volcano, Alaska. *Journal of Volcanology and Geothermal Research*, *189*(1-2), 12–18. doi: 10.1016/j.jvolgeores.2009.10.002

Ching, E. J., Bornhoft, B., Lasemi, A., & Ihme, M. (2022). Quail: A lightweight open-source discontinuous Galerkin code in Python for teaching and prototyping. *SoftwareX*, *17*, 100982. doi: 10.1016/j.softx.2022.100982

Chouet, B. A., & Matoza, R. S. (2013). A multi-decadal view of seismic methods for detecting precursors of magma movement and eruption. *Journal of Volcanology and Geothermal Research*, *252*, 108–175. doi: 10.1016/j.jvolgeores.2012.11.013

Coppess, K. R., Dunham, E. M., & Almquist, M. (2022). Ultra and very long period seismic signatures of unsteady eruptions predicted from conduit flow models. *Journal of Geophysical Research: Solid Earth*, e2022JB024313. doi: 10.1029/2022JB024313

Costa, A. (2005). Viscosity of high crystal content melts: Dependence on solid fraction. *Geophysical Research Letters*, *32*(22). doi: 10.1029/2005GL024303

Dmitrieva, K., Hotovec-Ellis, A. J., Prejean, S., & Dunham, E. M. (2013). Frictional-faulting model for harmonic tremor before Redoubt Volcano eruptions. *Nature Geoscience*, *6*(8), 652–656. doi: 10.1038/ngeo1879

Fee, D., Haney, M. M., Matoza, R. S., Van Eaton, A. R., Cervelli, P., Schneider, D. J., & Iezzi, A. M. (2017). Volcanic tremor and plume height hysteresis from Pavlof Volcano, Alaska. *Science*, *355*(6320), 45–48. doi: 10.1126/science.aah6108

Fee, D., Izbekov, P., Kim, K., Yokoo, A., Lopez, T., Prata, F., ... Iguchi, M. (2017). Eruption mass estimation using infrasound waveform inversion and ash and gas measurements: Evaluation at Sakurajima Volcano, Japan. *Earth and Planetary Science Letters*, *480*, 42–52. doi: 10.1016/j.epsl.2017.09.043

Fowler, A., Scheu, B., Lee, W., & McGuinness, M. (2010). A theoretical model of the explosive fragmentation of vesicular magma. *Proceedings of the Royal Society A: Mathematical, Physical and Engineering Sciences*, *466*(2115), 731–752. doi: 10.1098/rspa.2009.0382

Freret-Lorgeril, V., Bonadonna, C., Corradini, S., Donnadieu, F., Guerrieri, L., Lacanna, G., ... others (2021). Examples of multi-sensor determination of eruptive source parameters of explosive events at Mount Etna. *Remote Sensing*, *13*(11), 2097. doi: 10.3390/rs13112097

Gestrich, J. E., Fee, D., Tsai, V. C., Haney, M. M., & Van Eaton, A. R. (2020). A physical model for volcanic eruption tremor. *Journal of Geophysical Research: Solid Earth*, *125*(10), e2019JB018980. doi: 10.1029/2019JB018980

Gonnermann, H. M. (2015). Magma fragmentation. *Annual Review of Earth and Planetary Sciences*, *43*(1), 431–458. doi: 10.1146/annurev-earth-060614-105206

Gonnermann, H. M., & Manga, M. (2003). Explosive volcanism may not be an inevitable consequence of magma fragmentation. *Nature*, *426*(6965), 432–435. doi: 10.1038/nature02138

Gonnermann, H. M., & Manga, M. (2007). The fluid mechanics inside a volcano. *Annu. Rev. Fluid Mech.*, *39*, 321–356. doi: 10.1146/annurev.fluid.39.050905.110207

Gualda, G. A., Cook, D. L., Chopra, R., Qin, L., Anderson, A. T., & Rivers, M. (2004). Fragmentation, nucleation and migration of crystals and bubbles in the Bishop Tuff rhyolitic magma. *Earth and Environmental Science Transactions of The Royal Society of Edinburgh*, *95*(1-2), 375–390. doi: 10.1017/S0263593300001139

Gualda, G. A., & Ghiorso, M. S. (2013). The bishop tuff giant magma body: an alternative to the standard model. *Contributions to Mineralogy and Petrology*, *166*, 755–775. doi: 10.1007/s00410-013-0901-6

Gualda, G. A., & Rivers, M. (2006). Quantitative 3D petrography using x-ray tomography: Application to Bishop Tuff pumice clasts. *Journal of Volcanology and Geothermal Research*, *154*(1-2), 48–62. doi: 10.1016/j.jvolgeores.2005.09.019

Hess, K., & Dingwell, D. B. (1996). Viscosities of hydrous leucogranitic melts: A non-Arrhenian model. *American Mineralogist: Journal of Earth and Planetary Materials*, *81*(9-10), 1297–1300.

Hildreth, W., & Wilson, C. J. (2007). Compositional zoning of the Bishop Tuff. *Journal of Petrology*, *48*(5), 951–999. doi: 10.1093/petrology/egm007

Hobbs, P. V., Radke, L. F., Lyons, J. H., Ferek, R. J., Coffman, D. J., & Casadevall, T. J. (1991). Airborne measurements of particle and gas emissions from the 1990 volcanic eruptions of Mount Redoubt. *Journal of Geophysical Research: Atmospheres*, *96*(D10), 18735–18752. doi: 10.1029/91JD01635

Hotovec, A. J., Prejean, S. G., Vidale, J. E., & Gomberg, J. (2013). Strongly gliding harmonic tremor during the 2009 eruption of Redoubt Volcano. *Journal of Volcanology and Geothermal Research*, *259*, 89–99. doi: 10.1016/j.jvolgeores.2012.01.001

Jones, T. J., Cashman, K. V., Liu, E. J., Rust, A. C., & Scheu, B. (2022). Magma fragmentation: a perspective on emerging topics and future directions. *Bulletin of Volcanology*, *84*(5), 45. doi: 10.1007/s00445-022-01555-7

Kanamori, H., Mori, J., & Harkrider, D. G. (1994). Excitation of atmospheric oscillations by volcanic eruptions. *Journal of Geophysical Research: Solid Earth*, *99*(B11), 21947–21961. doi: 10.1029/94JB01475

Kasimov, A. R., & Gonchar, A. R. (2021). Reactive Burgers model for detonation propagation in a non-uniform medium. *Proceedings of the Combustion Institute*, *38*(3), 3725–3732. doi: 10.1016/j.proci.2020.07.149

Kazahaya, R., Mori, T., Takeo, M., Ohminato, T., Urabe, T., & Maeda, Y. (2011). Relation between single very-long-period pulses and volcanic gas emissions at Mt. Asama, Japan. *Geophysical research letters*, *38*(11). doi: 10.1029/2011GL047555

Konstantinou, K. I., & Schlindwein, V. (2003). Nature, wavefield properties and source mechanism of volcanic tremor: a review. *Journal of Volcanology and Geothermal Research*, *119*(1-4), 161–187. doi: 10.1016/S0377-0273(02)00311-6

Koyaguchi, T., Scheu, B., Mitani, N. K., & Melnik, O. (2008). A fragmentation criterion for highly viscous bubbly magmas estimated from shock tube experiments. *Journal of volcanology and geothermal research*, *178*(1), 58–71. doi: 10.1016/j.jvolgeores.2008.02.008

Lavallée, Y., & Kendrick, J. E. (2021). A review of the physical and mechanical properties of volcanic rocks and magmas in the brittle and ductile regimes. *Forecasting and planning for volcanic hazards, risks, and disasters*, 153–238.

doi: 10.1016/B978-0-12-818082-2.00005-6

Liu, C., Klostermeyer, J., Yeh, K., Jones, T., Robinson, T., Holt, O., ... others (1982). Global dynamic responses of the atmosphere to the eruption of Mount St. Helens on May 18, 1980. *Journal of Geophysical Research: Space Physics*, *87*(A8), 6281–6290. doi: 10.1029/JA087iA08p06281

McGuinness, M., Scheu, B., & Fowler, A. (2012). Explosive fragmentation criteria and velocities for vesicular magma. *Journal of volcanology and geothermal research*, *237*, 81–96. doi: 10.1016/j.jvolgeores.2012.05.019

McNutt, S. R. (1994). Volcanic tremor amplitude correlated with eruption explosivity and its potential use in determining ash hazards to aviation. In *Volcanic ash and aviation safety: Proceedings of the first international symposium on volcanic ash and aviation safety* (pp. 377–385).

McNutt, S. R., & Nishimura, T. (2008). Volcanic tremor during eruptions: Temporal characteristics, scaling and constraints on conduit size and processes. *Journal of Volcanology and Geothermal Research*, *178*(1), 10–18. doi: 10.1016/j.jvolgeores.2008.03.010

Melnik, O., & Sparks, R. (2002). Modelling of conduit flow dynamics during explosive activity at Soufrière Hills Volcano, Montserrat. *Geological Society, London, Memoirs*, *21*(1), 307–317. doi: 10.1144/GSL.MEM.2002.21.01.14

Morgavi, D., Laumonier, M., Petrelli, M., & Dingwell, D. B. (2022). Decrypting magma mixing in igneous systems. *Reviews in Mineralogy and Geochemistry*, *87*(1), 607–638. doi: 10.2138/rmg.2022.87.13

Mori, T., & Burton, M. (2009). Quantification of the gas mass emitted during single explosions on Stromboli with the SO2 imaging camera. *Journal of Volcanology and Geothermal Research*, *188*(4), 395–400. doi: 10.1016/j.jvolgeores.2009.10.005

Nakashima, Y., Heki, K., Takeo, A., Cahyadi, M. N., Aditiya, A., & Yoshizawa, K. (2016). Atmospheric resonant oscillations by the 2014 eruption of the Kelud Volcano, Indonesia, observed with the ionospheric total electron contents and seismic signals. *Earth and Planetary Science Letters*, *434*, 112–116. doi: 10.1016/j.epsl.2015.11.029

Pamukcu, A. S., & Gualda, G. A. (2010). Quantitative 3D petrography using x-ray tomography 2: Combining information at various resolutions. *Geosphere*, *6*(6), 775–781. doi: 10.1130/GES00565.1

Pamukcu, A. S., Gualda, G. A., & Anderson Jr, A. T. (2012). Crystallization stages of the Bishop Tuff magma body recorded in crystal textures in pumice clasts. *Journal of Petrology*, *53*(3), 589–609. doi: 10.1093/petrology/egr072

Pankhurst, M., Dobson, K., Morgan, D., Loughlin, S., Thordarson, T., Lee, P., & Courtois, L. (2014). Monitoring the magmas fuelling volcanic eruptions in near-real-time using X-ray micro-computed tomography. *Journal of Petrology*, *55*(3), 671–684. doi: 10.1093/petrology/egt079

Papale, P. (1999). Strain-induced magma fragmentation in explosive eruptions. *Nature*, *397*(6718), 425–428. doi: 10.1038/17109

Perugini, D., & Poli, G. (2012). The mixing of magmas in plutonic and volcanic environments: analogies and differences. *Lithos*, *153*, 261–277. doi: 10.1016/j.lithos.2012.02.002

Popa, R.-G., Bachmann, O., & Huber, C. (2021). Explosive or effusive style of volcanic eruption determined by magma storage conditions. *Nature Geoscience*, *14*(10), 781–786. doi: 10.1038/s41561-021-00827-9

Prejean, S. G., & Brodsky, E. E. (2011). Volcanic plume height measured by seismic waves based on a mechanical model. *Journal of Geophysical Research: Solid Earth*, *116*(B1). doi: 10.1029/2010JB007620

Raponi, M., Vilar, O., Arboleas, H., García, S., Otero, L., Pereyra, A., ... Gómez, M. (2021). First portable scanning-DOAS system developed in Latin America for volcanic SO2 monitoring. *Journal of South American Earth Sciences*, *108*,

103177. doi: 10.1016/j.jsames.2021.103177

Reath, K., Pritchard, M., Roman, D. C., Lopez, T., Carn, S., Fischer, T. P., ... others (2021). Quantifying eruptive and background seismicity, deformation, degassing, and thermal emissions at volcanoes in the United States during 1978–2020. *Journal of Geophysical Research: Solid Earth*, *126*(6), e2021JB021684. doi: 10.1029/2021JB021684

Ripepe, M., De Angelis, S., Lacanna, G., & Voight, B. (2010). Observation of infrasonic and gravity waves at Soufrière Hills Volcano, Montserrat. *Geophysical Research Letters*, *37*(19). doi: 10.1029/2010GL042557

Salisbury, M. J., Bohrson, W. A., Clynne, M. A., Ramos, F. C., & Hoskin, P. (2008). Multiple plagioclase crystal populations identified by crystal size distribution and in situ chemical data: Implications for timescales of magma chamber processes associated with the 1915 eruption of Lassen Peak, CA. *Journal of Petrology*, *49*(10), 1755–1780. doi: 10.1093/petrology/egn045

Scheu, B., & Dingwell, D. B. (2022). Magma fragmentation. *Reviews in mineralogy and geochemistry*, *87*(1), 767–800. doi: 10.2138/rmg.2021.87.16

Tepley III, F., Davidson, J., & Clynne, M. (1999). Magmatic interactions as recorded in plagioclase phenocrysts of Chaos Crags, Lassen Volcanic Center, California. *Journal of Petrology*, *40*(5), 787–806. doi: 10.1093/petroj/40.5.787

Vulpiani, G., Ripepe, M., & Valade, S. (2016). Mass discharge rate retrieval combining weather radar and thermal camera observations. *Journal of Geophysical Research: Solid Earth*, *121*(8), 5679–5695. doi: 10.1002/2016JB013191

Zhu, L., & Rivera, L. A. (2002). A note on the dynamic and static displacements from a point source in multilayered media. *Geophysical Journal International*, *148*(3), 619–627. doi: 10.1046/j.1365-246X.2002.01610.x